

PARADOXICALLY SPARSE CHEMOSENSORY TUNING IN
BROADLY-INTEGRATING EXTERNAL GRANULE CELLS
IN THE MOUSE ACCESSORY OLFACTORY BULB

APPROVED BY SUPERVISORY COMMITTEE

Dr. Julian P. Meeks

Dr. Brad E. Pfeiffer (Chair)

Dr. Todd F. Roberts

Dr. Wei Xu

Dr. Ilya Bezprozvanny

DEDICATION

I would like to thank the members of my Graduate Committee for their advice.

I would like to thank my advisor, Julian Meeks, for his unreserved help and guidance, without which this work would not be possible.

I give special thanks to my family and my dearest friend, Jiamin Sun, for their endless love and comfort which has supported me all along this twisting journey. And last, I dedicate this work to my childhood hero, the recently passed basketball legend, Kobe Bryant. His words and professional attitude have always inspired me to fulfill my potential. It is utterly heartbreaking to lose him and his talented daughter Gigi, at this young age. Rest in peace my friend.

PARADOXICALLY SPARSE CHEMOSENSORY TUNING IN
BROADLY-INTEGRATING EXTERNAL GRANULE CELLS
IN THE MOUSE ACCESSORY OLFACTORY BULB

by

XINGJIAN ZHANG

DISSERTATION / THESIS

Presented to the Faculty of the Graduate School of Biomedical Sciences

The University of Texas Southwestern Medical Center at Dallas

In Partial Fulfillment of the Requirements

For the Degree of

DOCTOR OF PHILOSOPHY

The University of Texas Southwestern Medical Center at Dallas

Dallas, Texas

May, 2020

Copyright

by

Xingjian Zhang, 2020

All Rights Reserved

PARADOXICALLY SPARSE CHEMOSENSORY TUNING IN
BROADLY-INTEGRATING EXTERNAL GRANULE CELLS
IN THE MOUSE ACCESSORY OLFACTORY BULB

Publication No. _____

Xingjian Zhang, Ph.D

The University of Texas Southwestern Medical Center at Dallas, Graduation Year

Supervising Professor: Julian Meeks, Ph.D.

Most terrestrial animal species heavily rely on non-volatile chemosignals for conspecific and heterospecific communication. The sensory system responsible for detecting such signals is especially important in guiding animal behavior. Such sensory system in rodents is called accessory olfactory system (AOS). The chemostimulation detection is done by the vomeronasal sensory neurons in the vomeronasal organ (VNO), with their ligand-specific receptors. The electrophysiological signals generated here are then projected to the accessory

olfactory bulb (AOB), where the local circuit performs preliminary filtering to the signal.

GABAergic interneurons are known to exert their signal sculpturing effect onto principal cells in many brain areas. However, the roles of the AOB GABAergic interneurons are poorly understood. Here, I focus on one genetically defined subtype of GABAergic interneuron, called external granule cell (EGC). Using fast non-ratiometric Ca^{2+} indicator GCaMP6f specifically expressed in target cell populations on a specialized *ex vivo* preparation that preserves the functional connections of VNO and AOB, I characterized and compared the tuning properties of EGC and the mitral cells (MC). EGCs show generally narrow tuning preferences towards naturalistic stimulation such as mouse fecal extract and urinal extract, but MCs are much more excitable upon monomolecular sulfated steroid ligands. The result on its appearance contradicts the integrative model as indicated by the circuitry architecture, in which individual EGC broadly connects with MCs by dendrodendritic reciprocal synapses.

One explanation is that EGC activation has relatively high threshold. In the presence of sulfated steroids, the excitatory inputs from the activated MCs may not be strong enough to elicit action potentials. Nevertheless, such inputs should be reflected by membrane potential recording of EGCs, in the form of subthreshold depolarizations. To verify this hypothesis, I performed *ex vivo* electrophysiological recording on EGCs upon the chemostimulation. As expected, subthreshold activities

were reliably triggered by sulfated steroid ligands, displaying a 'tuning' profile indistinguishable from that of MCs as indicated by GCaMP6f imaging.

AOB granule cells are widely believed to be the information gating module under various behavioral contexts. This unexpected discovery of EGCs might suggest a unique information processing logic of AOS fitting the purpose of rodent social communication.

TABLE OF CONTENTS

CHAPTER ONE INTRODUCTION.....	1
Pheromones are widely adopted communication vehicles	1
The nature of mouse pheromones.....	3
The detection and processing of pheromones	5
The stratified structure of the MOB and the AOB.....	10
The computation of inhibitory interneurons.....	12
The AOB inhibition and animal behaviors.....	15
CHAPTER TWO METHODOLOGY	19
Mice	19
Stimuli and reagents	19
Targeted GCaMP6f expression	20
VNO-AOB <i>ex vivo</i> preparation.....	22
2-photon <i>ex vivo</i> GCaMP6f imaging	23
Acute slice preparation	23
Electrophysiology.....	24
Data analysis	26
CHAPTER THREE RESULTS	30
Implementation of <i>ex vivo</i> AOB calcium imaging	30
Mitral cell GCaMP6f imaging confirms broad chemosensory integration.....	32
AOB juxtglomerular cells show a slight bias towards naturalistic stimuli.....	35
EGC GCaMP6f imaging indicates remarkably sparse chemosensory tuning ...	38
Chemosensory tuning comparisons between MC, JGCs and EGCs	42
GCaMP6f performance is not sufficient to explain the sparseness.....	45

<i>Ex vivo</i> EGC whole cell recordings reveal broad subthreshold responsiveness	52
The activation of EGCs under behavioral contexts	58
CHAPTER FOUR CONCLUSIONS AND RECOMMENDATIONS	65
Cell type-specific functional studies in the AOB <i>ex vivo</i> preparation.....	65
AOB EGCs are broadly innervated, but sparsely tuned to chemosensory stimuli	66
Implications for models of AOB information processing.....	71
Other questions and future directions	74
Concluding remarks	79
BIBLIOGRAPHY	80

PRIOR PUBLICATIONS

Zhang, X. and Meeks, J.P., 2019. Paradoxically sparse chemosensory tuning in broadly integrating external granule cells in the mouse accessory olfactory bulb. bioRxiv, 703892; doi: <https://doi.org/10.1101/703892> (under review, Journal of Neuroscience)

Wong, W. M., Cao, J., **Zhang, X.**, Doyle, W. I., Mercado, L. L., Gautron, L., and Meeks, J. P. 2019. Physiology-forward identification of bile acid sensitive vomeronasal receptors. bioRxiv, 766592; doi: <https://doi.org/10.1101/766592> (accepted by Science Advances)

Doyle, W.I., Dinser, J.A., Cansler, H.L., **Zhang, X.**, Dinh, D.D., Browder, N.S., Riddington, .M. and Meeks, J.P., 2016. Faecal bile acids are natural ligands of the mouse accessory olfactory system. Nature Communications, 7.

LIST OF FIGURES

FIGURE 1	5
FIGURE 2	6
FIGURE 3	9
FIGURE 4	15
FIGURE 5	30
FIGURE 6	32
FIGURE 7	34
FIGURE 8	35
FIGURE 9	37
FIGURE 10	39
FIGURE 11	41
FIGURE 12	44
FIGURE 13	46
FIGURE 14	47
FIGURE 15	48
FIGURE 16	49
FIGURE 17	50
FIGURE 18	51
FIGURE 19	53
FIGURE 20	55
FIGURE 21	57

FIGURE 22	57
FIGURE 23	59
FIGURE 24	60
FIGURE 25	62
FIGURE 26	63
FIGURE 27	77

CHAPTER ONE

Introduction

Pheromones are widely adopted communication vehicles

Pheromones, by the definition dated back to 1959 by Karlson & Luscher, are 'substances which are secreted to the outside by an individual and received by a second individual of the same species, in which they release a specific reaction' (Karlson and LÜScher, 1959). Since its first discovery in insects, pheromones have also been found in most vertebrates, including fish, amphibians, reptiles and mammals (Laberge and Hara, 2001; Dulac and Torello, 2003; Symonds and Elgar, 2008; Houck, 2009).

Pheromone-based social communication relies on the chemosensory systems. The chemosensation has been adopted by many animal species as a vital communication channel. Although visual signals and auditory signals are superior at information capacity and temporal and spatial resolution, some unique features of chemosensation make it one of the major sensory modalities for many species. First, the ligand-receptor pairs naturally give rise to the specificity. The diversity of ligand-receptor pairs enables them to convey a great multiplicity of information, and the binding specificity is indispensable for the system's reliability. Pheromones are both species- and gender- specific (Dulac and Torello, 2003). Like the codebook encryption of military telegraph, the species specificity is essential to secure the communication channel. The insect species usually has its specific pheromone repertoire to ensure species recognition and avoid interspecific attraction (McElfresh

and Millar, 2001). Interestingly, the encryption can also be cracked and exploited by predators and parasitoids (Stowe et al., 1995). The gender-specificity widely exists across many species. Female mice and male mice can have vastly different pheromone repertoires, and distinct behavioral response to the same pheromone (Dulac and Torello, 2003). Second, the conditions required by chemosignal production and diffusion are relatively 'inexpensive'. For example, invertebrates with small physical size or simple physiological structures, such as arthropods, widely adopt pheromone as their main communication vehicle. Aquatic animals adopt pheromones because water is not as ideal for the propagation of visual or acoustic signals as it is for the dissemination of chemosensory cues (Dulac and Torello, 2003). Even for animals living in extreme environments, for example *Proteus Anguinus*, a type of cave-dwelling salamander, pheromone remains to be a viable option (Guillaume, 2000). Third, many animals have evolved highly sensitive sensory systems for the pheromones. Mouse pheromone sensory system can be activated by concentrations as low as 10^{-11} M (Dulac and Torello, 2003), and male moth can detect sex pheromone at only a few hundred molecules per square centimeter (Wilson, 1963). The extreme sensitivity and the natural specificity make chemosignals much more noise-robust carriers for long-distance communication: moth pheromone traps reportedly have an effective attraction diameter of several hundreds of meters (Wall and Perry, 1987). Collectively, these unique advantages of

the chemosensory system make it the most widely adopted sensory modality in the animal kingdom.

The nature of mouse pheromones

The laboratory mouse also heavily relies on pheromones for intraspecies communication. Their pheromones widely exist in the urine, feces, saliva, tear and many other body secretions. The pheromone composition can be individually variable and state dependent (Liberles, 2014; Stowers and Liberles, 2016). As its definition states, pheromones are potent inducers of specific animal behaviors. Many vital behaviors such as mating behaviors, aggression towards intruders, maternal behaviors and individual recognition are mediated by the pheromones (Liberles, 2014).

Mouse pheromones feature a wide chemical diversity. In general, they can be divided into 2 major categories: small molecules and proteinaceous ligands (Liberles, 2014).

One major small molecule family is the steroid derivatives. Steroid derivatives are nonvolatile cues found in mouse body fluids. Secreted steroids contain the information about internal hormone state. Although solid evidence directly linking steroid derivatives with stereotyped mouse behaviors is lacking, these molecules correlate with the behavioral state of releaser and recipient animals. Physiology studies also confirmed that different subfamilies of steroid derivatives activate

discrete processing stream of the pheromone sensory system (Meeks et al., 2010; Hammen et al., 2014). In a more recent study, bile acids were identified from mouse feces as another ligand family (Doyle et al., 2016). Most of the small molecule ligands like steroid derivatives probably work in a combinatorial fashion. The individual compound's behavior inducing effect could be trivial.

Several proteinaceous pheromone families have been identified too. Certain proteinaceous pheromones by themselves reportedly are strong behavior inducers via labeled-line neural circuit on the recipient mouse. This type of pheromone is exemplified by several members of the exocrine gland-secreted peptide (ESP) family. ESP1, a male specific pheromone, induces female receptive behavior (Haga et al., 2010; Woodson et al., 2017). ESP22 from juvenile mouse reduces the mating acceptance of the female mice (Ferrero et al., 2013). A different proteinaceous ligand family is the major histocompatibility complex (MHC) peptides (Leinders-Zufall et al., 2004). The pheromonal function of MHC peptides remains undiscovered. The rich MHC heterogeneity is conjectured to contribute to mouse individual discrimination (Restrepo et al., 2006; Brennan, 2009), and evidence from mouse and other animal species supporting this hypothesis have accumulated in studies (Jordan and Bruford, 1998; Penn and Potts, 1998; Jacob et al., 2002; Cheetham et al., 2007; Leclaire et al., 2017). Major urinary protein (MUP) is another protein family that account for the majority of the mouse urinary proteins (Finlayson et al., 1965). MUPs evoke specific behaviors including aggression, scent countermarking and

attraction (Hurst et al., 1998; Dey et al., 2015; Stowers and Liberles, 2016). The combinatorial diversity of expression of MUPs were believed to be one of the physiological foundations of mouse individual recognition, in addition to the MHCs, but this view has been challenged by some other studies (Thoß et al., 2016).

The detection and processing of pheromones

Pheromone detection depends on the olfactory system (Fig. 1). Mouse olfactory system consists of 2 major subsystems: the main olfactory system (MOS) and the accessory olfactory system (AOS) (Dulac and Torello, 2003; Liberles, 2014). Smaller sensory substructures such as Grueneberg Ganglion (GG) are activated in certain olfactory conditions, but these substructures are not within my focus here.

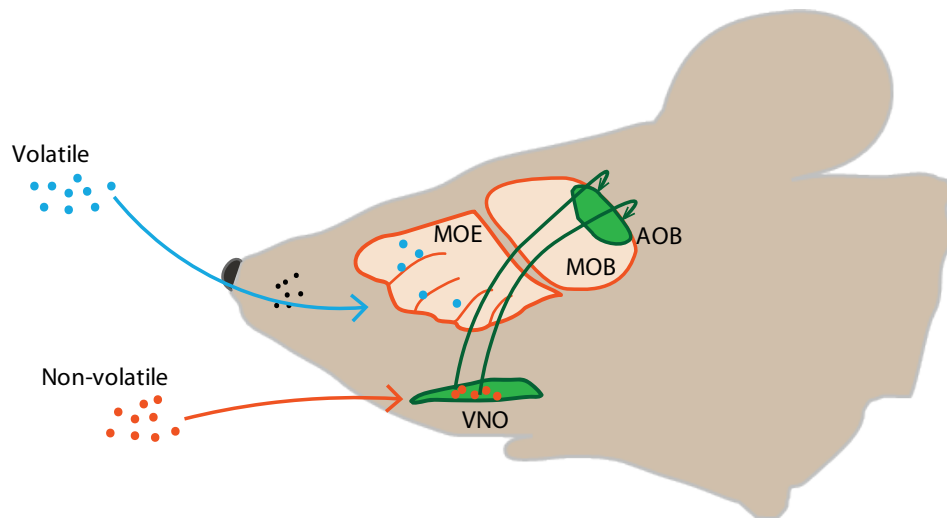


Figure 1. Mouse main olfactory system (MOS) and accessory olfactory system (AOS). Abbreviations: main olfactory epithelium (MOE); main olfactory bulb (MOB); accessory olfactory bulb (AOB); vomeronasal organ (VNO).

Main Olfactory System

The MOS is responsible for detecting airborne chemicals. Olfactory receptor neurons (ORNs) in the main olfactory epithelium (MOE) detect the molecular ligands and generate the electrophysiological signals. In the MOE, there are 2 major families of G protein-coupled receptors (GPCR) functioning as chemosensory receptors: odorant receptors (ORs) and trace-amine associated receptors (TAARs) (Liberles, 2014). Individual OSN exclusively expresses one chemosensory receptor, forming the labeled-line representation of the chemosignals (Su et al., 2009; Nagayama et al., 2014). The signals are then projected from the MOE to the main olfactory bulb (MOB), where they go through the preliminary processing (Fig. 2).

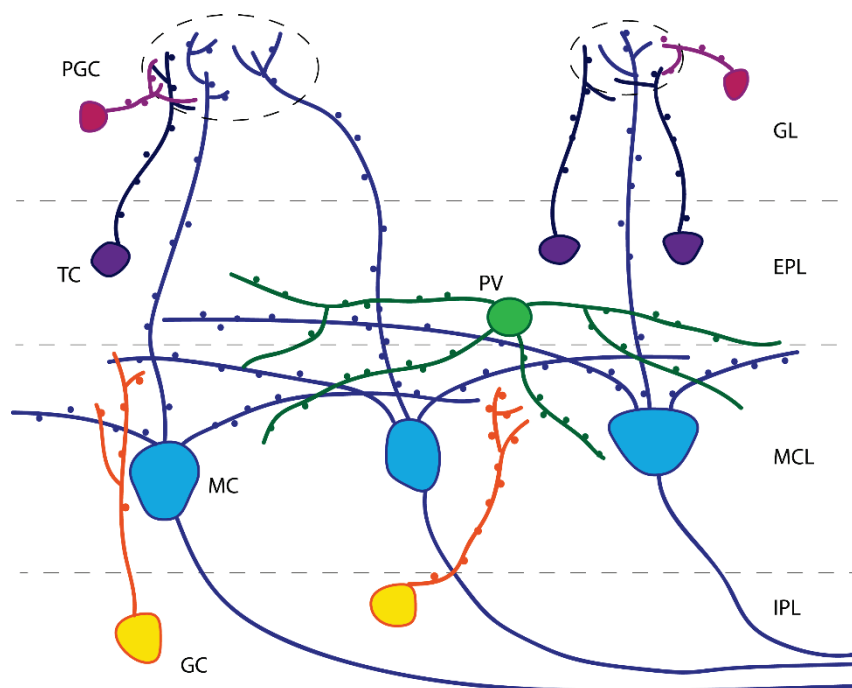


Figure 2. The circuit organization of the main olfactory bulb. Abbreviation: GL, glomerular layer; EPL, external plexiform layer; MCL, mitral cell layer; IPL, internal

plexiform layer; GCL, granule cell layer; PGC, periglomerular cell; TC, tufted cell; PV, parvalbumin expressing neuron; MC, mitral cell; GC, granule cell.

The principal cells in the olfactory bulb are mitral cells and tufted cells (M/T cells). These cells receive the MOE projection through their apical dendrites. Their long apical dendrites and the ORN projection axons form synaptic connections at olfactory glomeruli (Fig. 2). ORNs expressing the same olfactory receptor mostly converge onto one or two glomeruli, and most of the M/T cells receive excitatory input from one type of ORN projection (Su et al., 2009; Nagayama et al., 2014). The M/T cells project their efferent information to the piriform cortex, olfactory tubercle, entorhinal cortex and amygdala (Nagayama et al., 2014).

Accessory Olfactory System

The AOS is dedicated to detecting and processing nonvolatile chemicals (Mohrhardt et al., 2018). Most of the pheromones are nonvolatile chemicals existing in urine, feces, tear, and other bodily secretions (Liberles, 2014; Mohrhardt et al., 2018). Therefore, the AOS is the major pheromone processing system of the rodents.

The detection or the transduction is implemented by the vomeronasal receptor neurons (VRN) in the vomeronasal organ (VNO). The mouse VNO is a bonified capsule located symmetrically at the both sides of the lower part of the nasal septum. Inside the capsule is the crescent-shaped vomeronasal epithelium (VNSE) where VRNs reside. The chemical intake is through a duct that connects the VNO

and nasal cavity. Unlike the MOS where the intake of the airborne molecules is coupled with respiration, nonvolatile chemical intake requires a pumping mechanism powered by vasomotor movement (Meredith and O'Connell, 1979).

Similar to the ORNs in the MOE, most of the VRNs exclusively express one vomeronasal receptor (VR) type (Mohrhardt et al., 2018). VRs are also GPCRs. There are 2 major families of VRs: V1R and V2R. For the rodents, V1R family includes ~180 GPCRs with $G\alpha_{i2}$ subunit (Dulac and Axel, 1995). They are specialized in detecting small molecules such as urinary volatiles and sulfated steroids (Leinders-Zufall et al., 2000; Nodari et al., 2008; Isogai et al., 2011). The V2R is a family of ~120 GPCRs with $G\alpha_o$ subunit (Herrada and Dulac, 1997; Matsunami and Buck, 1997; Ryba and Tirindelli, 1997). Compared with V1Rs, V2Rs are featured with larger extracellular domains (Yoshinaga et al., 2013). V2Rs are specialized in detecting large molecules, mostly proteins and peptides. In pseudostratified VNSE, the V1R expressing neurons are confined to the apical region and the V2R expressing neurons are within the basal region (Shinohara et al., 1992; Berghard and Buck, 1996; Jia et al., 1997; Mohrhardt et al., 2018). A minor receptor family called formyl peptide receptors (FPRs) were also discovered in the AOB (Liberles, 2014). However, the function of this family remains largely elusive.

VRNs project their signals to the accessory olfactory bulb (AOB) (Fig. 3). The encoded information is preserved along the projection (Meeks et al., 2010; Tolokh et al., 2013). The V1R expressing neurons project to the anterior AOB (aAOB) while

the V2R expressing neurons project to the posterior AOB (pAOB) (Mohrhardt et al., 2018).

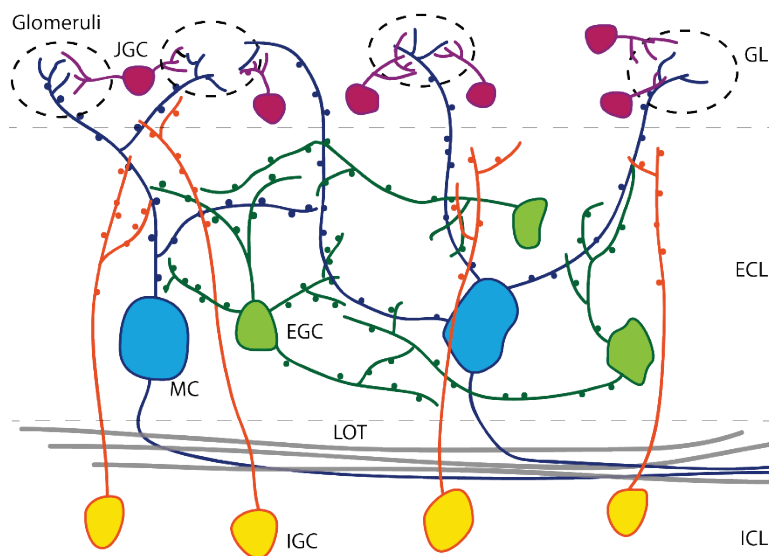


Figure 3. The circuit of mouse accessory olfactory bulb. Abbreviations: GL, glomerular layer; ECL, external cell layer; LOT, lateral olfactory tract; ICL, internal cell layer; JGC, juxtglomerular cell; EGC, external granule cell; MC, mitral cell; IGC, internal granule cell.

Alike the MOB, the mitral and tufted cells in the AOB receive the afferent signal from the VNO projection at the AOB glomeruli. The signals processed by the local circuit in the AOB are then sent to the downstream targets including amygdala, bed nucleus of stria terminalis (BNST) (Liberles, 2014). Notably, the AOB projection bypasses the olfactory cortex and directly goes to the hypothalamic areas that regulate various hormones, therefore potentially direct innate behaviors including mating, aggression, paternal behavior, etc. (Dulac and Torello, 2003; Liberles, 2014; Mohrhardt et al., 2018).

The stratified structure of the MOB and the AOB

The local circuits in the MOB (Fig. 2) and AOB (Fig. 3) are the first processing center for the MOS and the AOS respectively. The general architectures of the MOB and AOB share the similar stratified organization (Jia et al., 1999). M/T cells receive chemosensory inputs from the sensory organ (MOE or VNO) in the glomerular layer. There is however, one key difference between the MOS and AOS. The projections of the MOE to the MOB are thought to be monotypic (Fig. 2), i.e. each M/T cell is exclusive to 1 type of chemoreceptor (Su et al., 2009), but the projection from the VNO to the AOB can be monotypic or heterotypic (Wagner et al., 2006) (Fig. 3).

Like many other brain areas, the signal is also tightly modulated by the GABAergic interneurons. There are myriad GABAergic interneuron subtypes in the olfactory bulb.

The most abundant interneuron in the MOB glomerular layer is the juxtglomerular cells (JGC) (Larriva-Sahd, 2008; Maksimova et al., 2019). The JGC is a heterogeneous family, with several morphologically distinguishable subtypes (Nagayama et al., 2014). In the MOB, some of the subtypes project their dendrites exclusively to 1 glomerular but certain others such as the superficial short-axon cells have their dendrites in the interglomerular space (Nagayama et al., 2014). The AOB glomerular layer also homes JGCs (Fig. 3) (Larriva-Sahd, 2008).

In the MOB, the principal cells (M/T cells) reside in the mitral cell layer (MCL) or the external plexiform layer. In the proximity of the M/T cells, there are several

interneuron subtypes described, of which parvalbumin (PV) expressing neuron stands out being well-studied. PV expressing neurons account for ~30% of the entire population of cortical GABAergic interneurons (Tremblay et al., 2016). PV expressing neurons are a group of morphologically heterogeneous neurons, which can be further divided into short axon cells, Van Gehuchten cells, multipolar-type cells, inner short-axon cells and innerhorizontal cells (Nagayama et al., 2014). The EPL-PV neurons reciprocally interact with the M/T cells. They receive glutamatergic excitatory inputs and send feedback inhibition to the M/T cells (Nagayama et al., 2014). EPL-PV neurons are recognized as the global normalizer of the MOB circuit (Kato et al., 2013). In the next section, I will elaborate the computations of interneurons.

Likewise, the AOB ECL (MCL in Fig. 3) also homes a type of GABAergic interneurons, named external granule cell (EGC) (Larriva-Sahd, 2008). Relative to the MOB PV neurons, EGCs are poorly studied. Morphologically, EGCs are characterized by the small soma size (~10 μm), axonless configuration and far-reaching spine-rich dendrites (Larriva-Sahd, 2008). They widely form dendrodendritic reciprocal synapses with the mitral and tufted cells in the ECL (Castro et al., 2007; Larriva-Sahd, 2008; Moriya-Ito et al., 2013). The role of EGCs in the AOB local circuit remains elusive, largely due to the lack of well-characterized molecular markers to target these neurons.

The layer beneath the mitral and tufted cells, is occupied mainly by GABAergic granule cells. The layer is the granule cell layer (GCL) in the MOB (Nagayama et al., 2014) (Fig. 2), and internal cell layer (ICL) in the AOB (Larriva-Sahd, 2008)(Fig. 3). Morphologically, 3 types of cells with distinct dendritic configurations were found in the MOB GCL in early studies: type-I, type-II and type-III (Nagayama et al., 2014). In the AOB ICL, the most conspicuous type is the internal granule cell (IGC) (Larriva-Sahd, 2008; Maksimova et al., 2019). These cells are featured with long ascending dendrites that reaches and resolve in the ECL (Larriva-Sahd, 2008), forming reciprocal dendrodendritic synapses with the mitral cells as well (Larriva-Sahd, 2008; Cansler et al., 2017; Maksimova et al., 2019).

The computation of inhibitory interneurons

A system built with only excitation is both unstable and limited at the computational power (Kepecs and Fishell, 2014). The inhibitory modules are crucial in that they maintain the stable status and simultaneously enrich the signal diversity, enhance the robustness and render the specificity.

Although some inhibitory interneurons are projection neurons, most are confined within local circuits, making synaptic connections with local principal neurons or other interneurons (Kepecs and Fishell, 2014; Tremblay et al., 2016). The inhibitory interneurons have remarkable diversity in terms of the morphology,

connectivity and physiological properties, but their functional diversity may be defined within a number of stereotypes (Kepecs and Fishell, 2014).

The foremost function of the inhibitory interneurons is maintaining the homeostasis between excitation and inhibition (E/I balance) and prevent runaway firing (Kepecs and Fishell, 2014; Tremblay et al., 2016; Ferguson and Gao, 2018). A recent scrutiny of zebra fish revealed tightly and precisely coupled excitation and inhibition (Rupprecht and Friedrich, 2018), increase and decrease together in physiological activities. At the system level of information processing, a balanced E/I seesaw is required for the information capacity and noise robustness (Rubin et al., 2017). The disruption of the E/I balance is also strongly correlated with the psychiatric disorder (Kepecs and Fishell, 2014).

At the level of the neural computation, inhibitory interneurons are considered as the arithmetic modules responsible of operations such as division and subtraction (Isaacson and Scanziani, 2011; Kepecs and Fishell, 2014). Their modulation helps filter out noise, improves fidelity, sharpen the tuning, render specificity to the neural signal and pace the oscillation (Isaacson and Scanziani, 2011). Neural circuit motif, a widely accepted model in which modulatory functions are attributed to specific repeated connectivity patterns of specific cell types, is employed to bridge the neuronal physiology to the circuit behaviors (Braganza and Beck, 2018). Specific inhibitory interneuron subtypes with their target cells form highly stereotypic

computation motifs, such as feedback inhibition, feedforward inhibition, disinhibition, etc.

Conventionally, inhibitory interneurons are classified by their expression of certain molecular markers. Parvalbumin (PV), somatostatin (SOM) and 5HT3aR conveniently divide the majority of the inhibitory neurons into three groups with little overlap (Tremblay et al., 2016). Upon the genetic fingerprints, interneurons are further characterized by their morphology, connectivity pattern, synaptic properties and intrinsic firing properties (Kepecs and Fishell, 2014). For example, many of the PV neurons are fast-spiking basket cells and chandelier cells that target the soma or the axon initial segment of the principal cells (Tremblay et al., 2016). The functions of the interneuron in the circuitry are based upon their fundamental properties. PV neurons are often found broadly sampling the global activity and regulate principal cell firing through their divisive feedback inhibition (Isaacson and Scanziani, 2011; Wilson et al., 2012; Kato et al., 2013). The MOB EPL-PV neuron is a typical population. EPL-PV neurons are broadly driven by the glutamatergic excitatory inputs from the M/T cells (Kato et al., 2013; Miyamichi et al., 2013). Each EPL-PV neuron integrates signals from multiple MCs, therefore are much more broadly tuned to the chemicals relative to the M/T cells (Fig. 4). The feedback inhibition from PV neurons is proportionate to the MC activity (Fig. 4). Its net effect is the normalization of the global M/T cell activities with little change on their tuning preferences (Isaacson and Scanziani, 2011; Kato et al., 2013). Similar configuration was also

reported in other sensory cortices such as the primary visual cortex (Wilson et al., 2012).

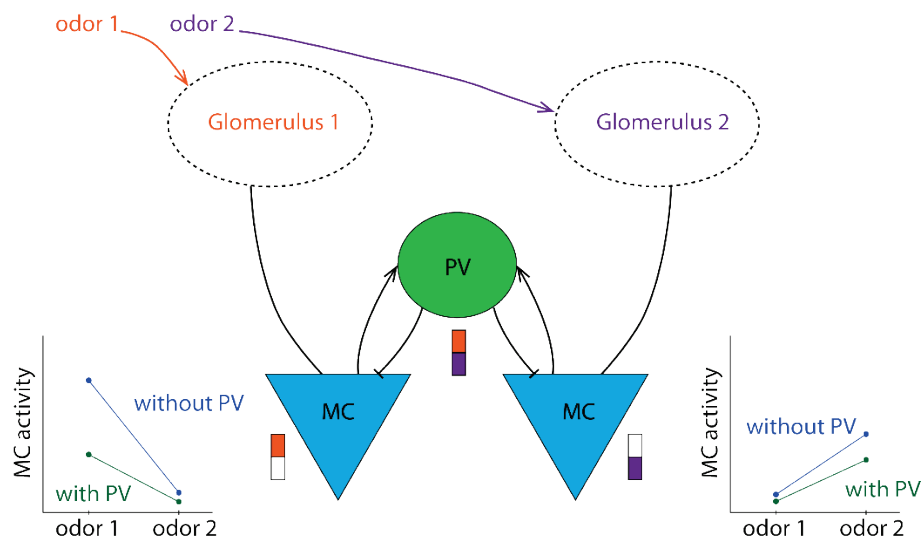


Figure 4. MOB PV neurons integrate inputs from multiple MCs and impose divisive feedback inhibition.

The AOB inhibition and animal behaviors

The inhibitory interneurons in the AOB circuitry remain poorly understood. Nevertheless, the importance of the AOB inhibition has long been acknowledged. Female mouse forms a long-term memory of her mating pair after only one sexual encounter (Kaba and Nakanishi, 1995; Keverne and Brennan, 1996; Brennan, 2001; Brennan, 2009). This mating memory is manifested in the Bruce effect (pregnancy block), in which a mated female tends to terminate their pregnancy following the exposure to an unfamiliar male (Keverne and Brennan, 1996; Brennan, 2009). This long-term memory relies on the AOS, but not the MOS (Lloyd-Thomas and Keverne, 1982).

Some experimental clues tend to attribute this mating to the inhibitory circuit of the AOB. Social encounters were found to enhance the excitability of granule cells (Cansler et al., 2017; Gao et al., 2017). Strengthened GABAergic transmission was observed after mating (Brennan et al., 1995; Kaba and Nakanishi, 1995; Matsuoka et al., 1997; Kaba and Huang, 2005). On the other hand, disruption of the GABAergic transmission in the AOB could cause the shift of MC tuning preference (Hendrickson et al., 2008), or even failure of pregnancy as reported in an early study (Kaba and Keverne, 1988). These observations support a prevailing model that attributes the formation of the mating memory to the AOB MC-interneuron plasticity (Brennan, 2009).

Despite that this model can be used to explain AOS-dependent animal behaviors, our understanding of its detail is poor. Particularly, the functional role of EGCs, one major GABAergic interneuron subtype, remains a blank. Hitherto, there is only one targeted research on these cells (Maksimova et al., 2019). EGCs noticeably share similar connectivity configurations with the EPL-PV neurons. They both reside in the same layer with the M/T cells, and broadly connected with the M/T cells. A natural hypothesis is that these cells function in a similar fashion with the EPL-PV neurons.

Here, in this research, I conducted the first targeted investigation of AOB EGCs in the context of chemosensory function, aiming to answer the question when and how these neurons are recruited to fire. I studied EGC function using two-photon

GCaMP6f Ca^{2+} imaging and patch clamp electrophysiology in a specialized *ex vivo* preparation that preserves functional connectivity between the VNO and AOB (Meeks and Holy, 2009). This preparation enabled direct observation of AOB neuronal activation by peripheral stimulation with known AOS activators, including monomolecular steroid ligands and natural ligand blends (mouse urine and feces). Using a Cre-expressing transgenic mouse (*Cort-Cre*), which selectively labels subsets of AOB EGCs (Taniguchi et al., 2011; Maksimova et al., 2019), I measured EGC activation by AOS activators, finding unexpectedly sparse activation compared to mitral cells (MCs) and JGCs. Because this observation was at odds with my expectations, I performed whole-cell patch clamp experiments on EGCs, ruling out the possibility that the tuning sparseness as revealed by the *ex vivo* imaging experiment is caused by a lower reporting efficiency of GCaMP6f in EGCs. Using whole-cell patch clamp recording on the *ex vivo* setup, I then confirmed the hypothesis that EGCs indeed broadly integrate from MCs by observing their broad innervations from the monomolecular ligands. EGCs rarely fire action potentials unless a natural blend containing many chemosensory cues (e.g. mouse urine or feces) was used to stimulate the VNO. These results indicate that AOB EGCs, unlike the MOB EPL-PVs, do not support divisive normalization in the context of small numbers of odorants, but instead inhibit MCs only in specific chemosensory conditions involving rich pheromone environments. These studies provide new

information about the role of AOB EGCs in AOS sensory processing, and place important constraints on the models of AOB circuit function.

CHAPTER TWO

Methodology

Mice

All animal procedures were in compliance with the UT Southwestern Institutional Care and Use Committee. Mice used in this research were C57BL/6J unless otherwise noted. *Cort*-T2A-Cre and *Gad2*-IRES-Cre (Taniguchi et al., 2011) were from The Jackson Laboratory (Stock# 010910 and 028867). *Pcdh21*-Cre (Nagai et al., 2005) mice were kindly shared by the laboratory of Timothy Holy with permission from the originating institution. Both male and female mice were used in all experiments and the results pooled. 27 mice (14 females and 13 males) were used for EGC Ca²⁺ imaging. 5 mice (3 females and 2 males) were used for JGC Ca²⁺ imaging. 9 mice (4 females and 5 males) were used for MC Ca²⁺ imaging. For slice electrophysiological experiments, 20 mice (17 females and 3 males) were used for EGC patch clamp recordings and cell-attached recordings; 10 mice (3 females, and 7 males) were used for MC patch clamp recordings and cell-attached recordings. For EGC *ex vivo* patch clamp recording, 16 mice (10 females and 6 males) were used.

Stimuli and reagents

Female mouse fecal extracts and urine were prepared as previously described (Nodari et al., 2008; Meeks et al., 2010; Doyle et al., 2016). Fecal extracts and urine were pooled across subjects of the same sex, strain, and age, then aliquoted and

stored at $-80\text{ }^{\circ}\text{C}$. Just prior to each experiment, aliquots were thawed and diluted in control Ringer's saline solution containing (in mM): 115 NaCl, 5 KCl, 2 CaCl_2 , 2 MgCl_2 , 25 NaHCO_3 , 10 HEPES and 10 glucose. For VNO stimulation, the fecal extracts were diluted at 1:300 and the urine was diluted at 1:100, concentrations that activate roughly equal number of AOB MCs in the *ex vivo* preparation (Doyle et al., 2014).

All sulfated steroids were purchased from Steraloids, Inc. (Newport, RI, USA). The sulfated steroid panel includes A7864 (5-androsten-3 β , 17 β -diol disulphate, disodium salt), A6940 (4-androsten-17 α -ol-3-one sulphate sodium salt), A7010 (4-androsten-17 β -ol-3-one sulphate, sodium salt), E0893 (1, 3, 5(10)-estratrien-3, 17 α -diol 3-sulphate, sodium salt), E1050 (1, 3, 5(10)-estratrien-3, 17 β -diol disulphate, disodium salt), E4105 (4-estren-17 β -ol-3-one sulphate, sodium salt), P3817 (5 α -pregnan-3 α -ol-20-one sulphate sodium salt), P3865 (5 α -pregnan-3 β -ol-20-one sulphate, sodium salt), P8168 (5 β -pregnan-3 α -ol-20-one sulphate, sodium salt), Q1570 (4-pregnen-11 β , 21-diol-3, 20-dione 21-sulphate, sodium salt) and Q3910 (4-pregnen-11 β , 17, 21-triol-3, 20-dione 21-sulphate, sodium salt). 20 mM stock solutions of A7864, E1050 and Q1570 were prepared in H_2O , the 20 mM stock solution of all other sulfated steroids were prepared in methanol. Upon use, stock solutions were diluted at 1:2000 into the Ringer's solution (10 μM working concentration). Methanol was diluted at 1:2000 into the Ringer's solution as a vehicle control.

Targeted GCaMP6f expression

GCaMP6f expression in AOB neurons was achieved by injecting AAV.CAG.Flex.GCaMP6f.WPRE.SV40 (Chen et al., 2013) to the corresponding Cre mouse lines. To achieve optimal GCaMP6f expression, different AAV pseudotypes were used. AAV9 (Penn Vector Core, Catalog #AV9-PV2816) was used on *Cort-T2A-Cre* for EGC labeling, and *Gad2-IRES-Cre* (Taniguchi et al., 2011) for JGC labeling. AAV5 (Penn Vector Core, Catalog #AV5-PV2816) was used on *Pcdh21-Cre* for MC labeling, confirming the efficacy of this AAV pseudotype for MCs (Rothermel et al., 2013).

Adult mice aged 8-12 weeks were used for virus injection. Intracranial injections were performed on a customized stereotaxic device that rotated the mouse head such that the rostral end of the head tilted up $\sim 30^\circ$. Mice were anesthetized via isofluorane inhalation using a SomnoSuite Small Animal Anesthesia System (Kent Scientific). For each animal, ~ 180 - 300 nL viral vector ($\geq 1e^{13}$ vg/ml) was injected into AOB. The bilateral coordinates, measured from the lambda, were lateral $\sim +1000$ μm , anterior $\sim +4150$ μm for 8-week adult mice. Depth coordinate was ~ 3300 μm beneath the skull surface. After virus injection, the animals were allowed to recover for at least 3 weeks before being used for experiments.

Additionally, the *Cort-T2A-Cre* mouse line crossed with Ai148D mice (TIT2L-GC6f-ICL-tTA2)-D (JAX stock #030328) to transgenically express GCaMP6f in EGCs. 8 of these animals were used in *ex vivo* imaging, producing 10 EGC data instances. I observed no discernible differences between the *ex vivo* GCaMP6f

imaging results of Ai148D animals and virally driven animals (data not shown), so these instances are compiled in one dataset and analyzed together.

VNO-AOB *ex vivo* preparation

Ex vivo preparations were performed as described previously (Meeks and Holy, 2009; Doyle et al., 2014). Briefly, mice were anesthetized by isoflurane inhalation, followed by rapid decapitation into the ice-cold aCSF. After removing the scalp, the snout and olfactory bulbs were separated from the rest of the skull, and the snout was then halved along the midline, maintaining the VNO AOB from the right hemisphere. The resulting tissue was affixed to a plastic plank with tissue adhesive (Krazy Glue, Elmer's Products) and placed into a custom perfusion chamber where secondary dissections were performed. In this chamber, room temperature (22-25 °C) oxygenated artificial cerebrospinal fluid (aCSF) was rapidly superfused over the tissue at a rate of 5-8 mL/min. aCSF contained (in mM): 125 NaCl, 2.5 KCl, 2 CaCl₂, 1 MgCl₂, 25 NaHCO₃, 1.25 NaH₂PO₄, 25 glucose, 3 *myo*-inositol, 2 sodium pyruvate, and 0.4 sodium ascorbate. The septal cartilage was carefully removed, exposing the septal tissue containing the axons from VNO to the oxygenated aCSF. The sample was then transferred to a second, custom-built tissue chamber with a rotatable platform. A small cut was made at the anterior end of the VNO capsule, through which polyimide tubing (A-M Systems, 0.0045"ID, 0.00050" WALL) was inserted for stimulus delivery. Stimulation solution was pressurized at 9-12 psi giving an effective flow rate of 0.2-1 mL/min. Valve opening was controlled by Automate Scientific

perfusion system with ValveLink8.2 controller. Once cannulated, the platform was rotated so that the AOB facing upward to facilitate 2-photon imaging on an upright microscope.

2-photon *ex vivo* GCaMP6f imaging

Adult mice aged 11-16 weeks were used for imaging. *Ex vivo* preparations in the customized chamber were placed into a custom adapter on a Thorlabs Acerra upright 2-photon microscope system equipped with an OLYMPUS XLUMPlanFLN 20X objective and a fast-scanning resonant galvanometer along one of the two principal axes. To excite GCaMP6f fluorescence, 910 nm light (average power 2100 mW measured at the laser, 25-35% power transmission for imaging) was used. Images with pixel dimensions 512x512 were acquired at 30 frames per second and synchronized with stimulus delivery system (Automate Scientific) via Axon Clampex 10 software (Molecular Devices). Episodic stimulation sessions, consisting of 1 s pre-stimulation VNO Ringer's solution flush, 8 s of VNO stimuli, and 11 s post-stimulation VNO Ringer's solution flush, were used to present multiple repeats per cell. Across sessions, stimulus presentation order was randomized to reduce the impact of potential stimulus order effects.

Acute slice preparation

Mice were anesthetized with isoflurane and immediately decapitated into ice-cold oxygenated aCSF with an additional 9 mM MgCl₂. Brains were then extracted

and a vertical cut at the prefrontal cortex was made and the anterior part containing the olfactory bulbs was preserved. Another vertical cut along the midline separated the two hemispheres, and both were embedded in aCSF containing 3% low-melt agarose at 37 °C. The agarose block was then mounted on an angled slicing platform on a vibrating microtome (Leica VT1200). The slicing blade ran at an angle of approximately 12 degrees off-sagittal, running from caudal/medial to rostral/lateral. The slices were then collected in recovery chamber containing oxygenated room-temperature aCSF with 0.5 mM kynurenic acid. Slices were allowed to recover at least 30 min before being used for patch clamp recording.

Electrophysiology

Whole-cell patch clamp recording

Acute slice electrophysiology was performed on the same upright 2-photon microscope used in *ex vivo* imaging. Slices were placed in a tissue chamber (Warner instruments), warmed to 28-30 °C by a temperature controller (Warner instruments). GCaMP6f-expressing neurons were identified using the same laser setup with *ex vivo* imaging. Thin borosilicate glass electrodes (TW150, World Precision Instruments) were pulled using a horizontal puller (P1000, Sutter Instruments). The electrodes were then filled with standard internal solution containing 115 mM K-gluconate, 20 mM KCl, 10 mM HEPES, 2 mM EGTA, 2 mM MgATP, 0.3 mM Na₂GTP, and 10 mM Na phosphocreatine at pH 7.37. AlexaFluor568 (166 μM, Thermo Fisher) was added for visualization under 2-photon

microscope. Pipette resistance ranged from 7-10 M Ω for EGC patch clamp, and 6-8 M Ω for MC patch clamp. The electrodes were controlled with a MicroStar motorized micro-manipulator (Scientifica). In the experiments probing the relationship between GCaMP6f signal and action potentials, after whole-cell configuration was formed, cells went through the voltage-clamp and current-clamp protocols. Our voltage-clamp protocol started at -70 mV, followed by a 10 s train of 5, 10 and 20 Hz depolarization pulses to 0 mV (2 ms pulse width). Under the current-clamp mode, I inject either sustained step currents or 2 ms current pulse trains at various amplitudes to evoke action potentials at desired frequencies. GCaMP6f signals were recorded simultaneously using the same imaging parameters as *ex vivo* Ca²⁺ imaging experiments. The GCaMP6f signal was then extracted using custom MATLAB programs.

Loose-seal cell-attached recording and local field stimulation

I used the same acute brain slice preparation for loose-seal cell-attached recordings as whole-cell patch clamp recordings. Pulse stimulation of the glomerular layer was applied using a stimulus isolator (World Precision Instruments A365) at 20 Hz for 10 s (5 ms pulse width). Stimulation was achieved via an ACSF-filled theta-glass electrode with a ~30 μ m tip. Spontaneous and evoked action potentials were recorded using ACSF-filled borosilicate glass pipettes (6-8 M Ω resistance) in the loose-seal configuration.

Ex vivo whole-cell patch clamp recording

The *ex vivo* preparation setup for whole-cell patch clamp experiments was the same as for the *ex vivo* imaging. *Cort*-T2A-Cre mice were crossed with Cre-dependent tdTomato effector mice (“Ai9” mouse line; Jackson Laboratory stock #007909) to label *Cort*⁺ cells. AlexaFluor488 (100 μM, Thermo Fisher) was added in the standard internal solution for electrode visualization under 2-photon microscope. Target cells were identified and approached using the ‘approach’ mode of the micro-manipulator (to facilitate penetrating the tissue without tearing the glomerular layer) prior to achieving the whole-cell configuration. After the whole-cell configuration was achieved, cells were held in current clamp mode. Upon break-in, the resting membrane potential of the cell was measured, and steady-state holding current was applied throughout the experiment to maintain the initial resting membrane potential. The same panel of monomolecular ligands and natural stimuli were applied to the VNO as the *ex vivo* Ca²⁺ imaging experiments.

All recordings were amplified via a MultiClamp 700B amplifier (Molecular Devices) at 20 kHz and were digitized by a DigiData 1440 analog-digital converter via pClamp 10.5 software (Molecular Devices, RRID: SCR_011323). Data were analyzed by custom software written in MATLAB and graphs were created using MATLAB and R (ggplot2).

Data analysis

Ex vivo 2-photon GCaMP6f imaging analysis

Raw 2-photon Ca^{2+} imaging analysis was performed using customized MATLAB scripts. ROIs were manually selected and $\Delta F/F$ values were extracted by comparing the change in fluorescence during stimulation to 30 frames (~ 1 s) prior to each stimulus session. Because EGCs were relatively rare in the field of view, and very dim at rest, before each experiment I manually pulsed the VNO with each of the stimuli in the panel, which revealed stimulus-responsive cells in the field of view. Throughout this study, only cells (MCs, EGCs and JGCs) that responded to at least one stimulus were included in the analysis. Further analysis of $\Delta F/F$ signals was performed using customized R scripts and graphs were made using ggplot2. $\Delta F/F$ responses were averaged over 4 or more trials for each stimulus. Because the latency to peak for each cell and each specific preparation can vary (typically between 7s and 12 s from stimulation onset), I used average response curves to determine a continuous series of samples during which the $\Delta F/F$ value is above 50% of the peak value. For each individual repeat, I integrated the $\Delta F/F$ intensity during this time window. I assessed the statistical reliability of each cell's stimulus responsiveness using the unpaired Student's *t*-test, comparing each stimulus to the vehicle control trials. I considered a cell to be responsive to a stimulus if (1) its *p*-value was less than 0.05 and peak $\Delta F/F$ was greater than 0.1 or (2) its *p*-value was less than 0.1 and peak $\Delta F/F$ greater than 0.3). For heat map displays throughout the manuscript (Fig. 7B, 9B, 11B), average peak $\Delta F/F$ value was used to represent each cell's response strength towards to each stimulation. Cumulative distribution of EGCs, JGCs and MCs tuning were evaluated using Kolmogorov–Smirnov test (Fig.

12A, 12B). Heat map displays of chemosensory tuning (e.g., Fig. 7B, Fig. 9B, Fig. 11B) were manually arranged based on each cells' ligand responsivity.

Simultaneous GCaMP6f imaging and acute brain slice electrophysiology

For analysis of voltage clamp stimulation experiments, $\Delta F/F$ responses to 5, 10, and 20 Hz pulse trains were pooled across cells and compared with Student's t-test (Fig. 14). For analysis of current clamp stimulation experiments, I measured the peak $\Delta F/F$ following each spike was measured, and $\Delta F/F$ -to-spike relationships were analyzed by 2-way ANOVA (Fig. 16). For loose-seal cell-attached recordings (Fig. 17, 18), electrical stimulation was used to stimulate the glomerular layer, resulting in variable spike timing in downstream neurons (i.e., total number of spikes and inter-spike interval distributions varied). For comparisons of the $\Delta F/F$ -spiking relationship in these experiments, I analyzed the first 20 consecutive spikes within the $\Delta F/F$ rising phase (i.e. prior to the overall peak/plateau). If a cell fired less than 20 spikes in a given trial, I analyzed the bout with the largest number of spikes. Average inter-spike intervals were 0.16 ± 0.01 s for MCs and 0.26 ± 0.09 s for EGCs. In these experiments, I measured the peak $\Delta F/F$ immediately following each spike and evaluated $\Delta F/F$ -to spiking performance using a 2-way ANOVA (Fig. 18). The average number of spikes to reach the 0.3 $\Delta F/F$ threshold was compared using Student's t-test (Fig. 18, right panel).

2-photon ex vivo whole-cell patch clamp electrophysiology analysis

In these experiments, each round of stimulation included 1 s pre-stimulation flush, 8 s stimulation and 11 s post-stimulation flush. The stimulation panel was split

into 2 bouts, each consisting of 6 sulfated steroids, 2 naturalistic stimuli, and the vehicle control, delivered in randomized orders. 2 bouts were used to cover the entire stimulation panel, and at least 3 full repeats of the full stimulus panel were used for all analyzed experiments. The membrane voltage was recorded at 20 kHz during the stimulation administration, and for all comparisons except spike analysis the data was downsampled by decimation by a factor of 100. For each repeat I calculated the average value of the top 5% of voltage reads in a static time window between 1.5 and 10 s following the stimulus onset and used the value to quantify the subthreshold activity. The response to each stimulus was compared to the vehicle control using the Wilcoxon rank sum test (Fig. 20, 21; 3 or more repeats per stimulus). All stimulus responses with $p < 0.05$ were considered effective. Comparisons of EGC and MC tuning distribution revealed by GCaMP6f imaging and EGC responsiveness revealed by *ex vivo* whole-cell patch clamp were conducted using Kolmogorov-Smirnov test (Fig. 21).

CHAPTER THREE

Results

Implementation of *ex vivo* AOB calcium imaging

The mouse AOB remains one of the most poorly understood principal sensory circuits in the mammalian brain. A large reason for this deficiency is the limited number of studies on the sensory responses of AOB neurons. Several *in vivo* and *ex vivo* studies have investigated MC sensory responses, but studies of interneuron function are severely lacking (Luo et al., 2003; Hendrickson et al., 2008; Ben-Shaul et al., 2010; Meeks et al., 2010; Doyle et al., 2016). I used combined *ex vivo* sensory preparations that retain VNO-AOB connectivity (Meeks and Holy, 2009) with 2-photon GCaMP6f imaging to measure Ca^{2+} signals in specific AOB neuronal populations (Fig. 5).

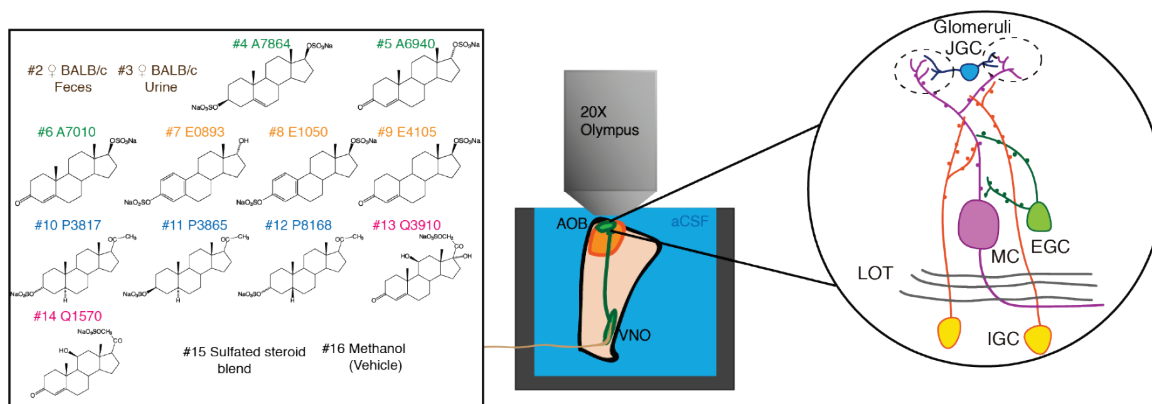


Figure 5. Overview of *ex vivo* Ca^{2+} imaging. Left: the stimulus panel delivered to the VNO to drive activity in the AOB. Included are natural ligand blends (1:100 diluted BALB/c mouse urine and 1:300 diluted mouse feces) and 11 monomolecular sulfated steroids at 10 μ M. Right: diagram of AOB circuit. MC: mitral cell, EGC: external granule cell, JGC: juxtglomerular cell, IGC: internal granule cell.

An important consideration for any study of chemosensory tuning is that measured receptive fields critically depend on the choice of chemosensory cues and concentrations. Some physiological studies of AOB tuning have exclusively utilized natural blends of chemosensory cues (e.g. dilute urine and saliva)(Hendrickson et al., 2008; Ben-Shaul et al., 2010; Tolokh et al., 2013), whereas others have used both of natural chemosignal blends and monomolecular VNO ligands (Meeks et al., 2010; Doyle et al., 2016; Doyle and Meeks, 2017). I chose to use both natural and monomolecular stimuli; I selected a panel that included diluted mouse urine and fecal extracts and monomolecular sulfated steroid ligands similar to those used by previous studies (Meeks et al., 2010; Turaga and Holy, 2012; Doyle et al., 2016). I first recorded sensory tuning to this panel of odorants in AOB MCs, by virally or transgenically driving GCaMP6f in *Pcdh21*-Cre transgenic mice (Nagai et al., 2005), I observed reliable, time-locked, stimulus-driven chemosensory activity in populations of AOB MCs across multiple stimulus trials (Fig. 6, Supplementary video 1). GCaMP6f responses to 8 s stimulus trials were large in amplitude ($\Delta F/F$ peak amplitude ~ 0.4 - ~ 3.2) and slow to peak and decay (peak time 7 to 12 s from stimulation onset; decay time 8 to 14 s), consistent with the time course of action potential firing observed in MCs with similar stimulation conditions (Hendrickson et al., 2008; Meeks and Holy, 2009). The establishment of GCaMP6f 2-photon Ca^{2+} imaging in the *ex vivo* preparation allowed us to investigate sensory tuning properties of genetically-defined AOB cell types.

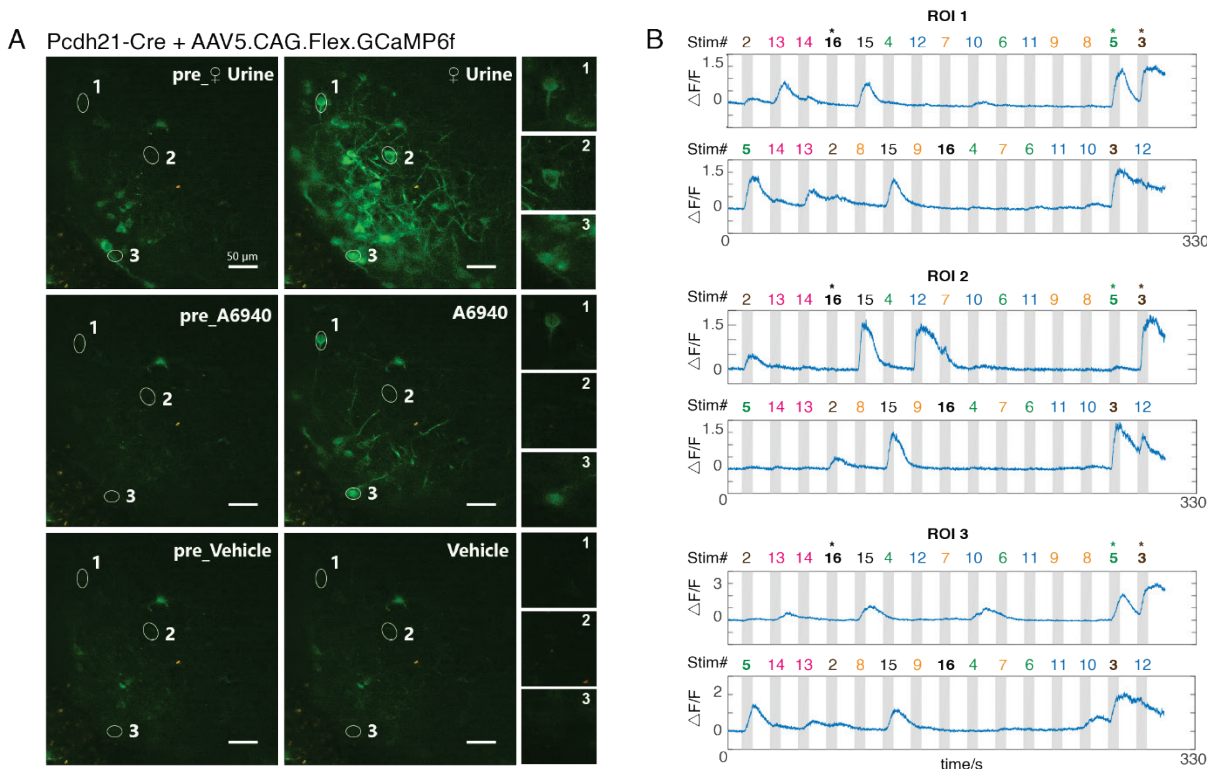


Figure 6. Ligand-elicited AOB neuron activities revealed by Ca^{2+} imaging. (A). Raw images of GCaMP6f fluorescence during ex vivo Ca^{2+} imaging experiments on AOB MCs. MCs expressed GCaMP6f via the infusion of Cre-dependent AAVs into the AOBs of *Pcdh21*-Cre transgenic mice 3 or more weeks prior to the recordings. Numbered regions of interest denote 3 highlighted MCs with different tuning preferences. **(B).** $\Delta\text{F}/\text{F}$ measurements from the 3 cells highlighted in (A) across 2 randomized repeats. Numbers above the gray vertical bars indicate the stimulus being applied, with colors matched to the stimulus panel in Fig. 5.

Mitral cell GCaMP6f imaging confirms broad chemosensory integration

AOB interneurons are principally excited by glutamatergic sensory input from AOB MCs (Brennan and Keiverne, 1997; Taniguchi and Kaba, 2001). The tuning of AOB MCs to a similar panel of chemosensory stimuli has been characterized using extracellular single-unit recordings (Meeks et al., 2010). However, since the GCaMP6f imaging platform represents a new approach, I first wanted to investigate

the tuning properties of genetically-defined MCs and compare these measurements to previous results (Fig. 7). Virally driven GCaMP6f expression was targeted in the MCs using *Pcdh21*-Cre mice. Strong baseline fluorescence was observed in cell bodies and apical dendrites of MCs spreading through the ECL and the glomerular layer (see Fig. 6A). I focused the recordings on GCaMP6f positive somas at the anterior AOB, where the V1R VSNs project to. All recorded cells were below the AOB glomerular layer (>70 μm from the AOB surface).

I recorded chemosensory activities of 266 AOB MCs (Fig. 7B), a cohort more than 2-fold larger than previous electrophysiological studies (Hendrickson et al., 2008; Ben-Shaul et al., 2010; Meeks et al., 2010; Tolokh et al., 2013). Consistent with previous results, dilute female mouse urine and feces stimulated strong global activity that began soon after stimulus delivery. Stimulation-evoked $\Delta F/F$ typically reached a peak within the first 2 seconds of an 8 s VNO stimulus delivery and displayed slow decay kinetics (decay time 8 – 12 s after the peak). Because the decay kinetics of GCaMP6f (Chen et al., 2013) are much faster than previous measurements of spike frequency decay, the slowness of GCaMP6f offset times likely reflects the slow cessation of spiking activity in AOB MCs (Luo et al., 2003; Wagner et al., 2006; Hendrickson et al., 2008; Ben-Shaul et al., 2010; Meeks et al., 2010; Mohrhardt et al., 2018).

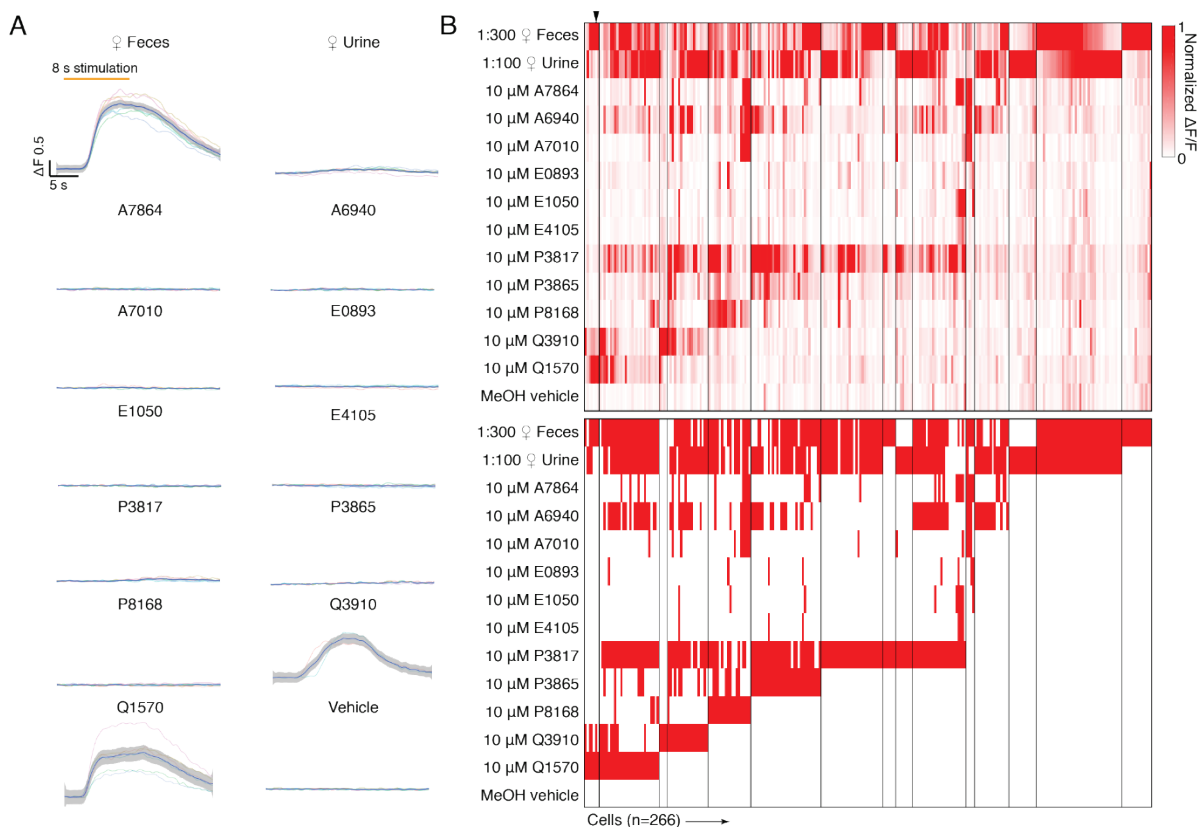


Figure 7. Chemosensory tuning of MCs. (A). Averaged response traces from an example MC. Traces were smoothed by local polynomial regression fitting. The shaded regions represent 95% confidence intervals. **(B).** Upper panel: heat map plot of normalized $\Delta F/F$ for 266 MCs. Lower panel: binary heat map plot of MC responsiveness; red tiles indicate a stimulus response that passed statistical criteria.

Of the 266 MCs I studied, 242 (91.0%) responded to at least 1 of the naturalistic stimuli, 199 (74.8%) responded to at least 1 monomolecular sulfated steroid ligand, and 125 (47.0%) were responsive to at least 2 sulfated steroids (Fig. 7, 8). I also observed a substantial number (24 of 266, 9%) of *Pcdh21+* cells that were exclusively responsive to one or more sulfated steroids (Fig. 7, 8). Cluster analysis of MC stimulus responses revealed stereotyped patterns of steroid sensitivity that were consistent with previous spiking-based measurements,

suggesting that MC GCaMP6f measurements accurately reflect MC activity (Fig. 7B)(Meeks et al., 2010).

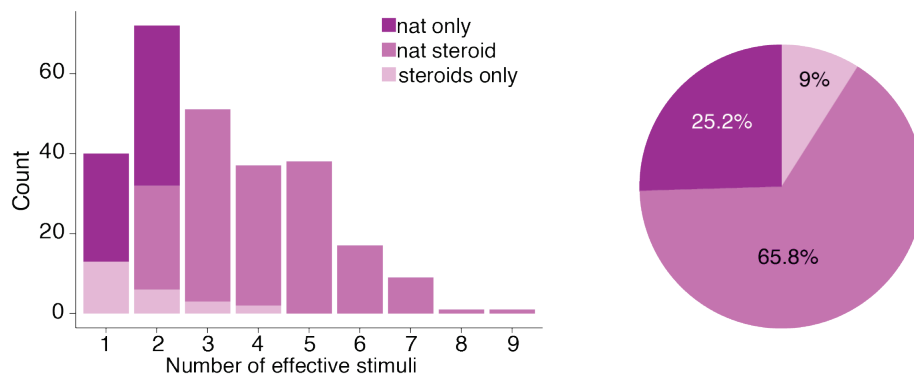


Figure 8. Distribution of MC tuning. **Left:** histogram showing the number of effective stimuli per cell. Recorded cells are classified into 3 color coded groups based on their responsivity. **Right:** pie chart showing the composition of recorded MC populations.

AOB juxtglomerular cells show a slight bias towards naturalistic stimuli

AOB MCs activity is shaped at multiple levels by inhibitory interneurons. The first stage of MC inhibition occurs in the glomerular layer, where AOB JGCs reside and release GABA onto MC dendrites and VSN presynaptic terminals (Mohrhardt et al., 2018). Because there have not been any systematic recordings of AOB interneuron tuning, I first sought to measure tuning in a general population of AOB GABAergic interneurons. I therefore expressed GCaMP6f in AOB interneurons by stereotaxically injecting AAV9.CAG.Flex.GCaMP6f into the AOB of *Gad2-IRES-Cre* transgenic mice (Taniguchi et al., 2011). A large population of neurons and dendritic arbors in the AOB glomerular layer and the superficial external cellular layer were strongly labeled and visible under the 2-photon microscope. The density of

GCaMP6f labeling in the deeper ECL, where EGC somas and IGC dendrites reside, paradoxically precluded the identification of well-resolved neuronal recordings.

However, neurons in the GL and superficial ECL were readily observed that had small soma size ($\sim 10 \mu\text{m}$) and compact dendrites that ramified within the glomerular layer, consistent with anatomical descriptions of JGCs (Larriva-Sahd, 2008).

JGCs reside in the glomerular layer and sense glutamate released by VSN axons and MC dendrites (Jia et al., 1999; Castro et al., 2007). As with MCs, following VNO chemosensory stimulation I observed large, reliable GCaMP6f responses over multiple randomized trials (Supplementary video 2). Noticeably, JGC GCaMP6f signals showed clear glomerular patches specific to the stimulus (Fig. 9A). Dilute BALB/c feces and urine were the two most potent JGC activators. 198 of 203 (97.5%) recorded JGCs showed reliable response towards female mouse feces or urine (Fig. 9B, C). In the JGC dataset, 300-fold diluted female mouse feces triggered stronger global activity than 100-fold diluted female mouse urine (Fig. 9B), which may at least be a partial consequence of the most accessible imaging region being in the lateral/anterior quadrant of the AOB. Of 113 (55.7%) sulfated steroid-responsive JGCs, 93 (45.8%) were responsive to no more than 2 different sulfated steroids and 9 (4.4%) were responsive to more than 4 sulfated steroids (Fig. 9C). The response patterns of AOB JGCs to this panel were largely similar to MCs, but a slightly lower percentage of JGCs responded to both naturalistic stimuli and monomolecular ligands than AOB MCs (Fig. 8, Fig. 9C), suggesting that, as

expected based on their restricted glomerular innervation patterns, JGCs perform less excitatory integration than MCs.

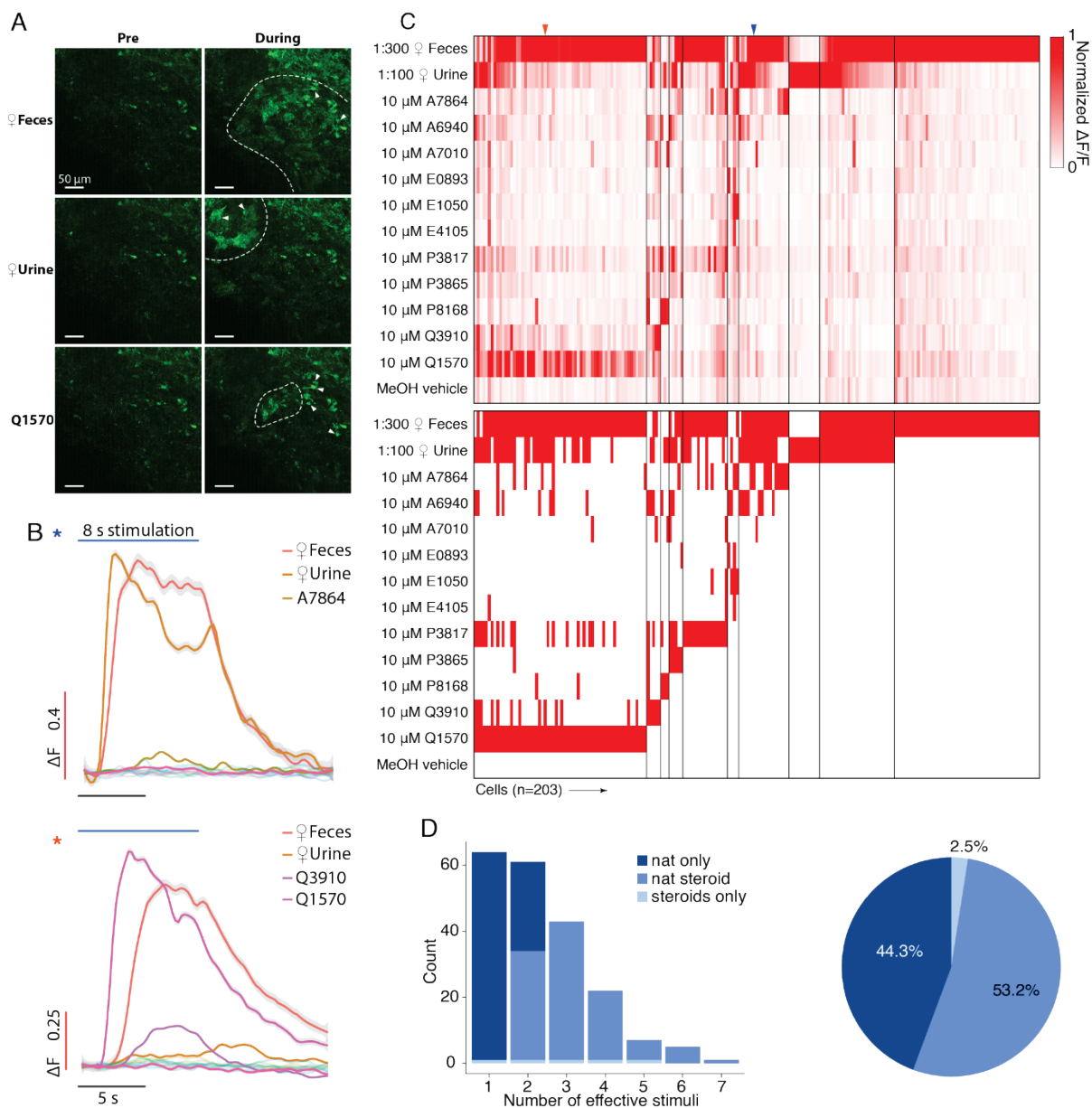


Figure 9. The tuning profile of AOB JGCs. (A). Example GCaMP6f images of the AOB Gad2+ JGCs under chemostimulation. Activated glomeruli are circumscribed by dashed lines. The scale bar marks 50 μ m. (B). Average $\Delta F/F$ traces for 3 example JGCs. Traces were smoothed by local polynomial regression fitting. The shaded regions indicate 95% confidence intervals. (C). Upper panel: heat map of

normalized $\Delta F/F$ for 203 JGCs. Lower panel: heat map of JGC stimulus responsiveness. (D). Left: histogram showing the number of effective stimuli per cell. Recorded cells were classified into 3 color coded groups by their selectiveness. Right: pie chart showing the composition of recorded JGC responsivities.

EGC GCaMP6f imaging indicates remarkably sparse chemosensory tuning

In primary chemosensory circuits, a common inhibitory motif involves broadly-integrating interneurons that perform divisive normalization or gain scaling (Wilson et al., 2012; Kato et al., 2013; Jeanne and Wilson, 2015). In the MOB, PV-EPL interneurons have been shown to perform these functions, but it is unknown whether analogous cells exist in the AOB. EGCs seemed well-matched to the morphological and physiological features of MOB PV-EPL neurons (Larriva-Sahd, 2008; Maksimova et al., 2019). Many EGCs are labeled in *Cort*-Cre transgenic mice (Maksimova et al., 2019), a fact which I exploited here to specifically target EGCs for viral infection (Fig. 10A). I drove GCaMP6f expression in *Cort*⁺ EGCs via AAV9.CAG.Flex.GCaMP6f injection into the AOB, followed by 2-photon Ca^{2+} imaging in *ex vivo* preparations.

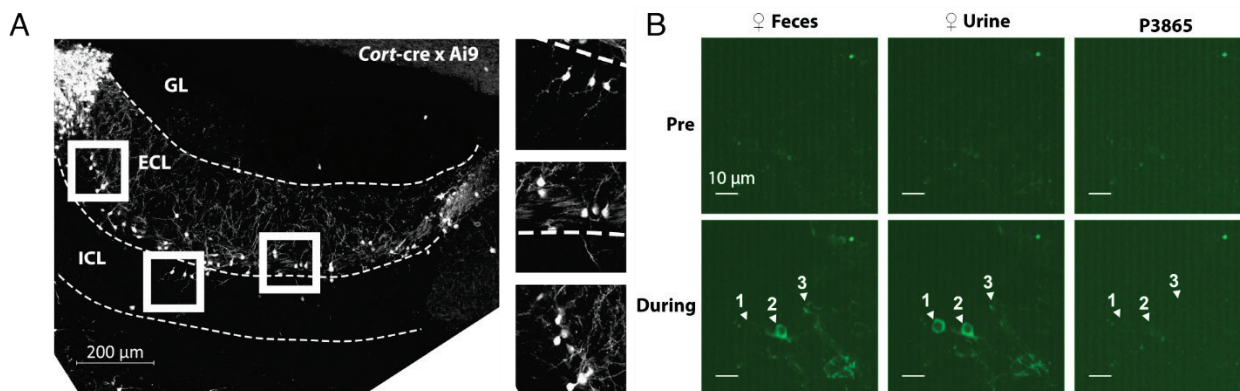


Figure 10. AOB Sagittal section from a *Cort-Cre* transgenic mouse mated to a cre-dependent tdTomato reporter line.

GCaMP6f expression was concentrated in the AOB ECL (> 80 μm from the AOB surface), but basal fluorescence intensity was extremely low compared to AOB cells infected with AAVs in both *Pcdh21-Cre* and *Gad2-Cre* mice (principal neurons and JGCs, respectively). Baseline GCaMP6f intensity was so low in most infected EGCs that they were not detectable above background until the AOB was activated by VNO stimulation (Fig. 10B, Supplementary video 3). Identified GCaMP6f-expressing cells had small soma size, unipolar or bipolar arborizations, and in cases where GCaMP6f fluorescence was extremely high (presumably due to loss of membrane integrity/cell death), I observed large arborizations dense in synaptic spines or gemmules, all of which were consistent with previous descriptions of EGCs (Larriva-Sahd, 2008; Maksimova et al., 2019).

I next investigated the chemosensory tuning properties of Cort+ EGCs towards the stimulus panel. The imaging field was focused on the anterior AOB, where the V1R sensory neurons project to. To my surprise, these EGCs showed evidence of

extremely sparse, rather than broad, tuning to the panel of chemosensory cues (Fig. 11B, C). Of the 65 recorded EGCs, 41 (63.0%) were activated only by naturalistic stimulation but not by sulfated steroids. Just 24 (37.0%) out of 65 Cort+ EGCs were responsive to sulfated steroids at all, with only 4 (6.2%) of the recorded cells exclusively activated by sulfated steroids (Fig 11B, C). This small population of cells showed broad sulfated steroid tuning, but also showed above-normal baseline fluorescence and spontaneous activity, perhaps suggesting that these cells may have been unhealthy (or are perhaps members of a rare Cort+ cell subtype). These experiments indicated that Cort+ EGCs have unique features that keep basal GCaMP6f fluorescence low and revealed that EGCs are sparsely tuned to chemical cues, which was contrary to my hypothesis that they, like PV-EPL interneurons in the MOB, are more broadly tuned than their upstream MC inputs.

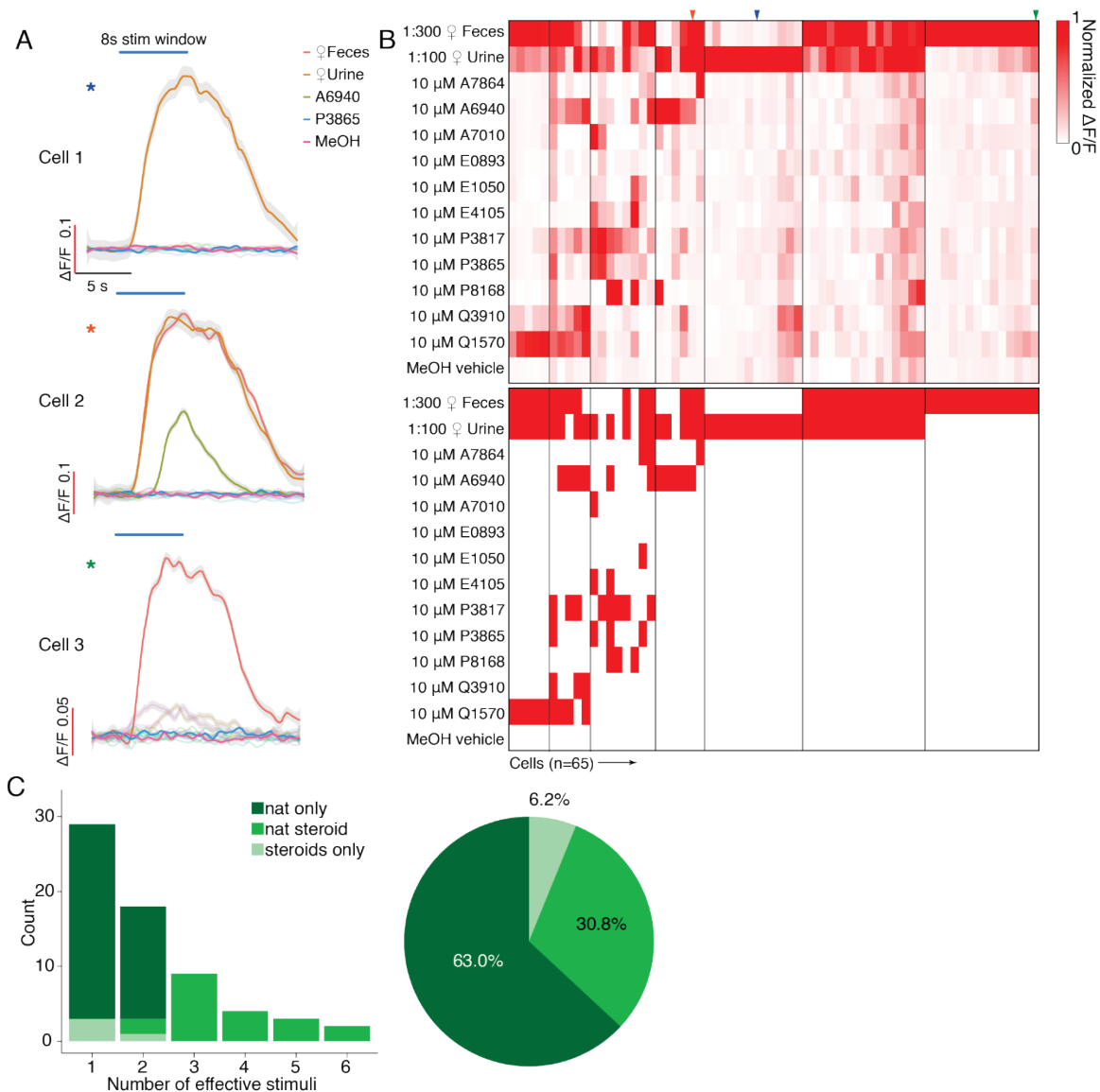


Figure 11. Chemosensory tuning of EGCs. (A). Averaged $\Delta F/F$ traces of the 3 cells shown in B. Traces were smoothed by local polynomial regression fitting. Shaded regions represent 95% confidence intervals. (B). Upper panel: heat map of normalized $\Delta F/F$ for 65 recorded EGCs. Lower panel: binary heat map of EGC stimulus responsiveness; red tiles represent the pairs that passed the statistical criteria. (C). Left: Histogram of EGC responsivity, with tuning classified into 3 color-coded subgroups. Right: Pie chart of EGC response classes.

Chemosensory tuning comparisons between MC, JGCs and EGCs

To more directly investigate cell type-specific tuning in the AOB, I assessed tuning breadth to all stimuli and monomolecular steroids across all of the cell types studied. (see Methods; Fig. 12). The distributions of effective stimuli with (Fig. 12A) or without (Fig. 12B) naturalistic stimuli per cell indicated that MCs demonstrated the broadest tuning to this panel of chemosensory cues, with 103 of 266 (38.7%) being responsive to no less than 4 stimuli (Fig. 12A), and 125 of 266 (47.0%) are responsive to no less than 3 sulfated steroids. In contrast, the majority of EGCs (47 of 65, 72.3%) were responsive to 2 or fewer stimuli and 41 of 65 (43.1%) were not responsive to any sulfated steroids tested. Gad2+ JGCs demonstrated intermediate tuning in both with and without naturalistic stimuli cases. The broadness of MC tuning is consistent with heterotypic integration of VNO inputs by AOB MCs (Wagner et al., 2006; Meeks et al., 2010). When natural ligand blends were included, the cumulative distributions of effective stimuli showed significant tuning differences between each interneuron type and MCs (EGC vs JGC, $p = 0.37$; EGC vs MC, $p = 1.5e-4$; JGC vs MC, $p = 4.9e-5$; Kolmogorov–Smirnov test; Fig. 12A). When naturalistic stimuli were excluded (Fig. 12B) these effects were even more pronounced (EGC vs JGC, $p = 0.063$; EGC vs MC, $p = 6.1e-7$; JGC vs MC, $p = 3.3e-5$; Kolmogorov–Smirnov test). EGCs, JGCs and MCs have similar distribution pattern across monomolecular steroid stimuli (Fig. 12C). For example, A6940, P3817, Q1570 and Q3910 activated the largest number of neurons in all three cell populations, while A7010, E0893, E1050 and E4105 activated the least number of

neurons. Overall, the tuning patterns observed to monomolecular sulfated steroids in all cell types were consistent with previous studies (Meeks et al., 2010; Turaga and Holy, 2012; Hammen et al., 2014).

JGC and EGC responses to natural ligand blends were overrepresented compared to MCs (Fig. 8, 9D, 11C). Specifically, 63.0% of EGCs (Fig. 11C), and 44.3% of JGCs (Fig. 9D) responded exclusively to natural ligand blends, compared to 25.2% for MCs (Fig. 8). Conversely, 9% of MCs are exclusively activated by sulfated steroids, compared to 6.2% of EGCs and 2.5% of JGCs. These differences in the proportion of responsive neurons may reflect complex network effects. However, they may more simply reflect differences in activation thresholds; previous studies indicated that MCs have higher signal/noise ratios and lower effective thresholds for activation than their VSN inputs (Meeks et al., 2010).

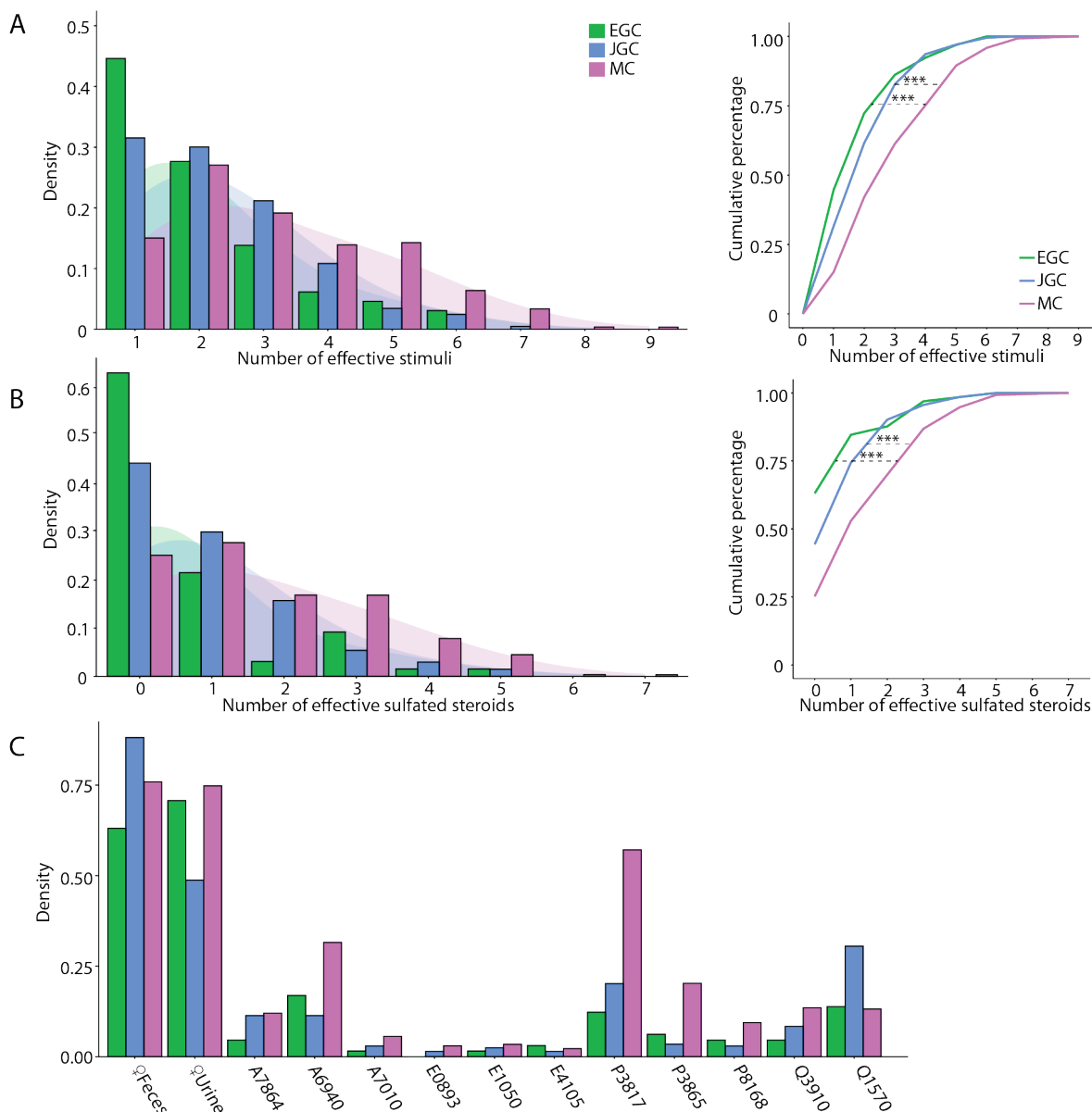


Figure 12. Comparison of 3 different cells' chemosensory distribution. (A). Left: histograms of the number of effective stimuli for EGCs, JGCs, and MCs. The shaded regions indicate Gaussian kernel densities. Right: cumulative distribution of the number of effective stimuli for each cell type. EGC vs MC, $p = 1.5e-4$; EGC vs JGC, $p = 0.37$; MC vs JGC, $p = 4.9e-5$, K-S test. **(B).** Same as in (A), with dilute urine and feces stimuli excluded. EGC vs MC, $p = 6.1e-7$; JGC vs MC, $p = 3.3e-5$; EGC vs JGC, $p = 0.063$, K-S test. **(C).** Percentage of EGCs, JGCs, and MCs that responded to each stimulus in the panel.

GCaMP6f performance is not sufficient to explain the sparseness

The observation that EGCs' chemosensory tuning is much sparser than MCs was contrary to my initial hypothesis. One possible explanation for this observation is that EGC GCaMP6f signals more weakly reflect spiking activity than in MCs. A standard method to verify the reporting efficiency is to perform simultaneous GCaMP6f imaging and whole-cell recording. To study spiking-GCaMP6f relationships, I first performed 2-photon guided whole-cell patch clamp recordings on EGCs and MCs while recording their GCaMP6f signals in acute brain slices. I first found that resting membrane potentials in EGCs ($-86.0 \text{ mV} \pm 1.0 \text{ mV}$, $n = 22$) were significantly hyperpolarized compared to MCs ($-63.7 \pm 1.0 \text{ mV}$, $n=18$), confirming earlier results (Gorin et al., 2016; Maksimova et al., 2019).

I investigated the GCaMP6f performance under the current clamp and the voltage clamp mode (Fig. 13).

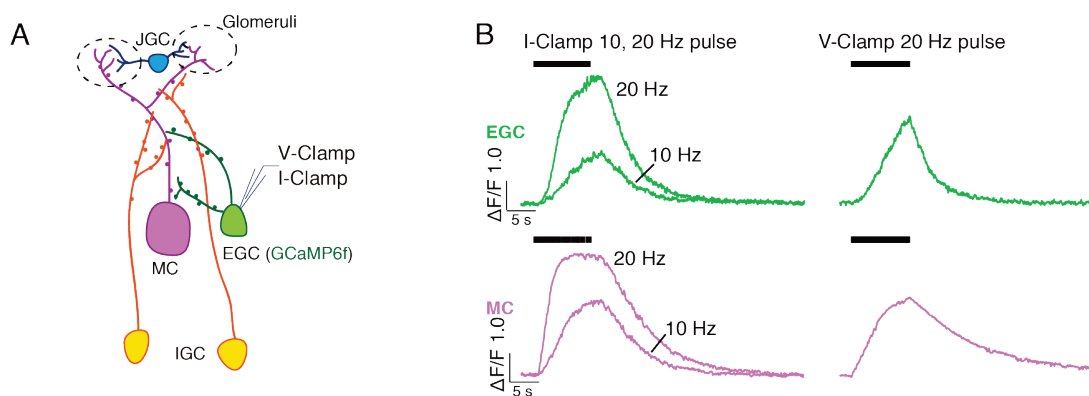


Figure 13. Assess GCaMP6f performance in EGC and MC using whole-cell patch clamp recording. (A). The diagram of the experiment setup. **(B).** Example GCaMP6f signals of EGC and MC under current clamp and voltage clamp pulsive stimulation.

In current clamp, both EGC and MC can reach to equally high peak $\Delta F/F$ level at 10-second 10 Hz and 20 Hz pulsive stimulation. However, under the voltage clamp 10-second 20 Hz depolarization pulse train, there are some noticeable differences. First of all, for both voltage and current clamp experiments, MCs showed faster rising dynamics than EGCs. Under voltage clamp, the $\Delta F/F$ of most of MCs (20 out of 22) showed a sigmoidal stimulus-response relationship, reaching a plateau by the end of the 10 s stimulation session (Supplementary video 4). In contrast, a significant fraction of EGCs (6 out of 17) did not reach a plateau in these same conditions (Supplementary video 5). Secondly, the peak $\Delta F/F$ value is statistically higher in MCs than EGCs (Fig. 14).

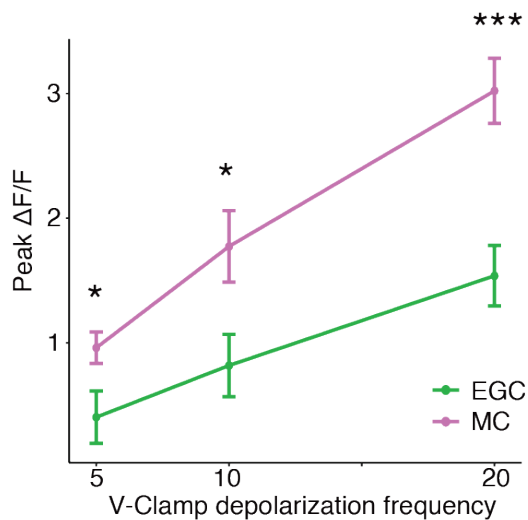


Figure 14. The peak $\Delta F/F$ levels of MCs are significantly higher than EGCs.

I then tested the GCaMP6f performance with step current injection under current clamp mode. Standardized ramps of current injection resulted comparable maximal spike frequencies in EGCs (N = 6, M = 27 Hz, SE = 1.53 Hz) and MCs (N = 4, M = 25 Hz, SE = 3.70 Hz; Fig. 15). I also observed that EGCs received high levels of excitatory synaptic input from MCs (Maksimova et al., 2019).

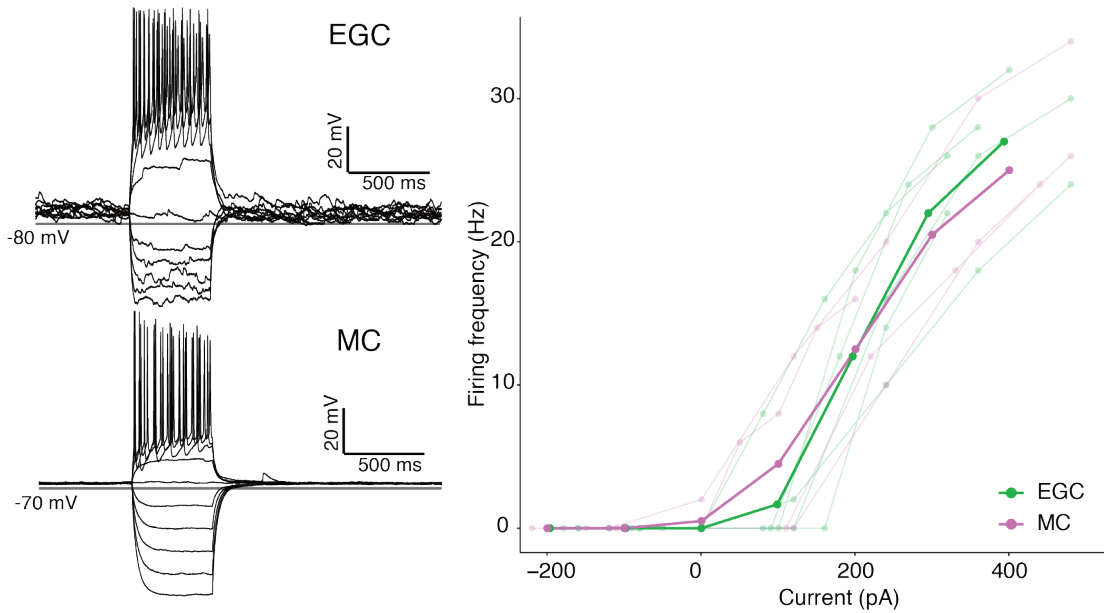


Figure 15. Standardized current injection protocols elicit similar frequencies of action potentials in example MC and EGCs. Left: Example step current injection tests of MC and EGC. **Right:** Input-output function of EGC and MC.

Semitransparent line plots on the background are current-output plots of individual cells (EGC: $N = 6$; MC: $N = 4$). The solid line plots are the average of the EGC and MC.

I then delivered a step current that reliably evoke ~ 10 Hz firing for 10 s (Fig. 16, right. MC: $N = 4$, $M = 9.64$ Hz, $SE = 0.131$ Hz; EGC: $N = 6$, $M = 10.07$ Hz, $SE = 0.256$ Hz; $p = 0.11$, student t test).

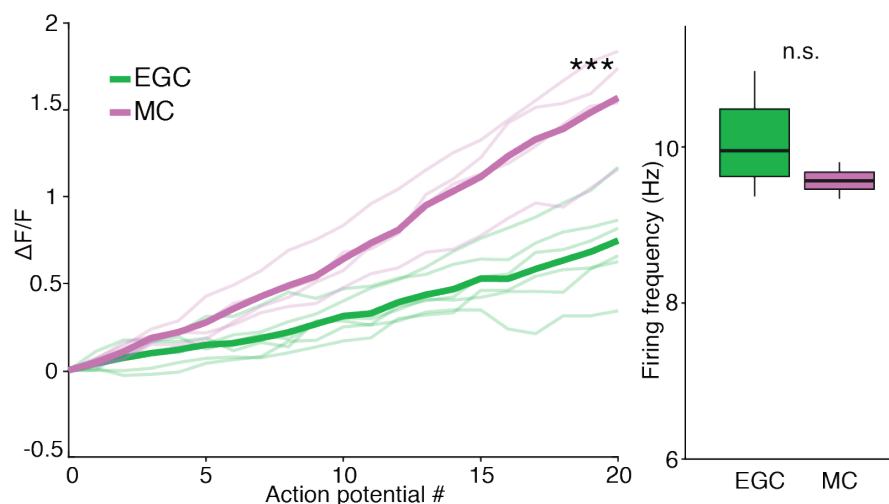


Figure 16. GCaMP6f signals under step current injection and ~10 Hz firing. **Left:** The $\Delta F/F$ -number-of-spikes relationship under ~10 Hz firing ($p = 5.06e-36$, main effect of cell type, two-way ANOVA). **Right:** Firing rate of EGC and MC (Student's t test, $p = 0.35$).

Unlike the pulse stimulation under voltage clamp, at the end of the stimulation session both cell types reached equally high peak $\Delta F/F$ (MC: $M = 3.68$, $SE = 0.267$; EGC: $M = 3.27$, $SE = 0.692$). I reason that the differences of my observations between voltage clamp and current clamp could be due to the different soma size (MC $\sim 20 \mu\text{m}$ vs EGC $\sim 10 \mu\text{m}$) (Larriva-Sahd, 2008) and higher input resistance of EGCs (Maksimova et al., 2019). I analyzed the $\Delta F/F$ -spike relationship of the first 20 spikes (Fig. 16, left). Both cell types showed near-linearity. Consistent with the faster rising dynamics of MCs, I observed a larger slope in MCs ($p = 5.01e-28$, two-way ANOVA). However, the measured reporting efficiency of GCaMP6f in EGCs is not low enough to fully account for the complete sparseness, let alone that the approximated spike- $\Delta F/F$ relationships are underestimation of the actual

relationships because my estimation does not take the delayed rising dynamics into account.

Patch-clamp based approaches for evaluating GCaMP6f-to-spiking relationships are common (Dana et al., 2019; Inoue et al., 2019; Wei et al., 2019), but have several important caveats. For example, whole-cell patch clamp disrupts cytoplasmic Ca^{2+} buffering environment. Moreover, stimulating spiking through the somatic patch clamp electrode does not activate these cells via the natural progression of synaptic excitation experienced *in vivo* (or the *ex vivo* preparation). In order to evaluate GCaMP6f performance during more natural waves of synaptic activation, I performed simultaneous GCaMP6f Ca^{2+} imaging and loose-seal cell-attached recordings while electrically stimulating the AOB glomerular layer (EGC: N = 8; MC: N = 12, Supplementary video 6, 7). In these recordings, both MCs and EGCs sometimes fired spontaneously, eliciting clear single-spike-triggered GCaMP6f responses (Fig. 17).

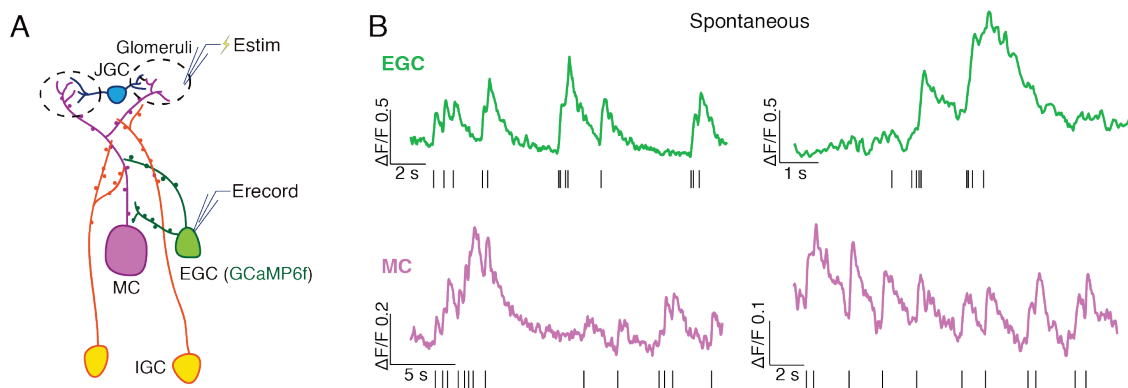


Figure 17. Assess GCaMP6f performance in EGC and MC using loose-seal cell-attached recording and local field stimulation. (A). The diagram of the experiment setup. **(B).** Example fluorescence traces showing spontaneous single spike evoked signals.

I also successfully recorded evoked postsynaptic action potentials in MCs and EGCs (Fig. 18. MC: N = 12, M = 8.76 Hz, SE = 1.87 Hz; EGC: N = 8, M = 12.63 Hz, SE = 3.50 Hz).

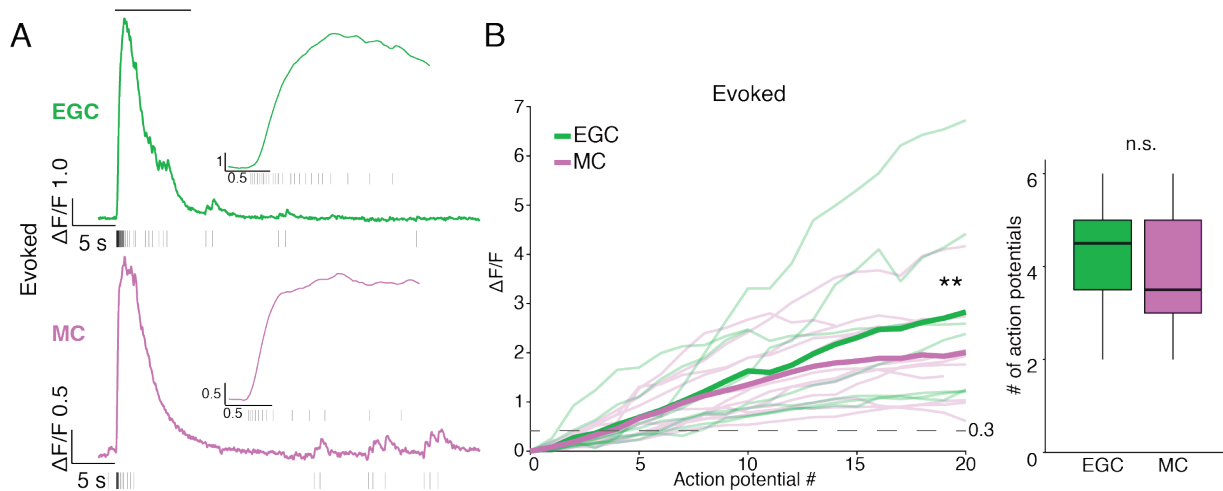


Figure 18. GCaMP6f signals under local field stimulation. (A) Example stimulation-evoked fluorescence response of EGC. Insets show the enlarged first 2 seconds after the onset of the stimulation. **(B). Left:** The $\Delta F/F$ -number-of-spikes relationship measured by loose-seal cell-attached recording ($p = 4.1e-3$, two-way ANOVA). **Right:** the number of action potentials required to pass $\Delta F/F = 0.3$ (Student's t test, $p = 0.66$).

Local field stimulation GCaMP6f in both cell types showed comparably high sensitivity (Fig. 18). On average, both cell types need around 4 spikes to surpass the $\Delta F/F$ criteria I used in determining the responsiveness in the *ex vivo* imaging experiments (Fig. 18B, EGC: N = 8, M = 4.13, SE = 0.52; MC: N = 12, M = 3.83, SE = 0.39; $p = 0.66$, student t test).

In summary, my whole-cell patch clamp and loose-seal cell attached recordings in EGCs and MCs have proved that the difference of GCaMP6f in these two cell types, if any, is not sufficient to explain the tuning sparseness of the EGCs.

***Ex vivo* EGC whole cell recordings reveal broad subthreshold responsiveness**

Measuring the relationships between spiking and $\Delta F/F$ in MCs and EGCs did not account for the sparseness of observed EGC tuning. Another possible explanation for EGC tuning sparseness could be EGCs' highly hyperpolarized resting membrane potentials, which my data and previous studies indicated is ~15-20 mV more hyperpolarized compared to other AOB neurons (Maksimova et al., 2019). This extreme resting hyperpolarization could prevent EGC spiking in all but the strongest stimulation conditions, potentially preventing the observation of robust GCaMP6f signals. I therefore performed 2-photon fluorescence-guided whole-cell patch clamp recordings on Cort+ EGCs in the *ex vivo* preparation (Fig. 19). I performed these experiments in *Cort-T2A-Cre* mice crossed to a cre-dependent tdTomato reporter line (Madisen et al., 2010), which improved my ability to identify EGC somata at rest. Using techniques similar to (Häusser and Margrie, 2013), I achieved the whole-cell configuration, then maintained each cell in current clamp near its initial resting potential via DC current injection. EGC resting membrane potentials in the *ex vivo* preparations, measured immediately after break-in, were depolarized compared to AOB slices (-63.7 ± 2.0 mV, $n = 18$). The reasons for the discrepancy were not clear, given that the internal and external solutions were identical to those in slice experiments. Nevertheless, I decided to maintain patched EGCs at these relatively depolarized potentials because they more likely reflected the state of EGCs in this *ex vivo* preparation. Importantly, the observation that EGCs

had relatively depolarized resting membrane potentials in the *ex vivo* preparation suggests that, if anything, EGCs in this preparation might be much closer to action potential threshold than was suggested by resting potentials measured in slice experiments.

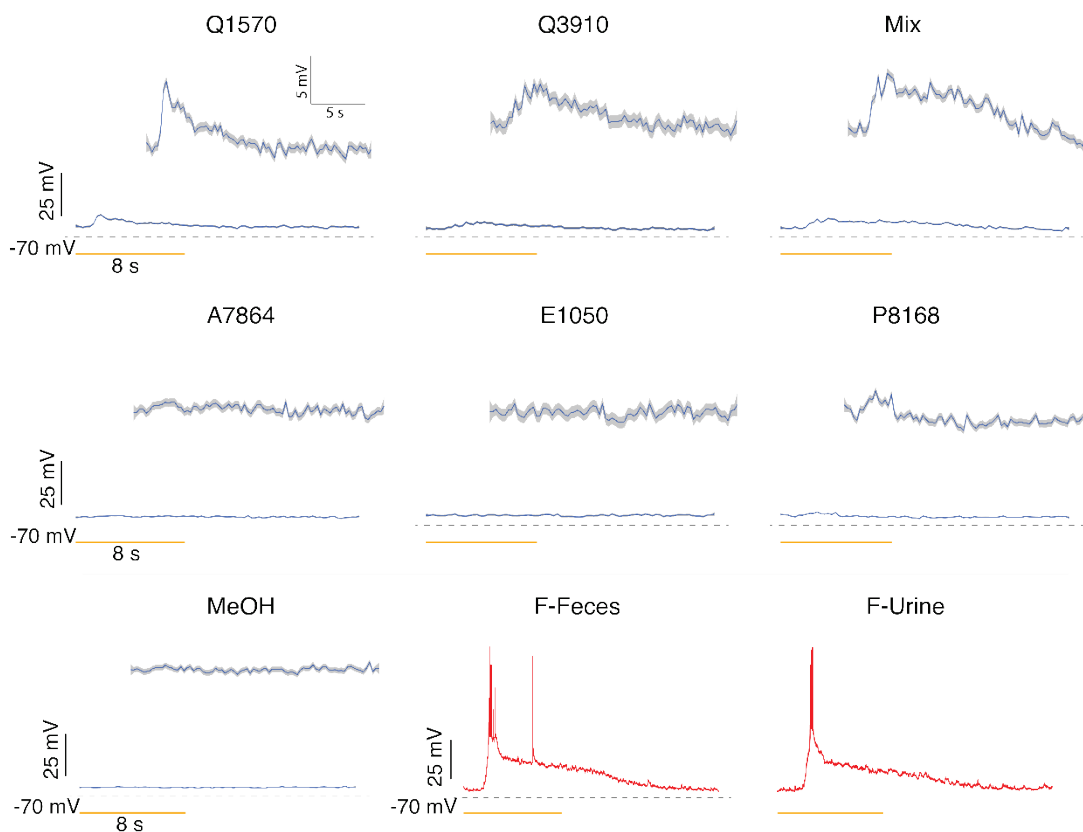


Figure 19. *Ex vivo* patch clamp recording of an example EGC. This example cell showed reliable subthreshold response to Q1570, Q3910, P8168 and the mixture of all sulfated steroids. The cell fired action potentials to feces and urine.

I proceeded recording EGC responses while I stimulated the VNO with the same panel of chemical cues used in GCaMP6f (Fig. 19). Consistent with GCaMP6f results, action potentials were reliably triggered in EGCs following VNO stimulation with dilute mouse urine or feces (natural ligand blends) but not by any

monomolecular ligands in the stimulation panel (Fig. 19). The spiking responses to peripheral stimulation typically included burst firing early in the stimulus presentation (11.90 ± 2.56 Hz, $n = 20$) followed by a long-lasting subthreshold decay period that extended well beyond the stimulation window (mean 90-10% decay time = 9.689 ± 0.436 s, $n = 76$ cell-stimulation pairs). The depolarization decay kinetics are comparable for naturalistic stimuli (mean 90-10% decay time = 10.255 ± 0.493 s, $n = 31$ cell-stimulation pairs) and monomolecular ligands (mean 90-10% decay time = 9.299 ± 0.651 s, $n = 45$ cell-stimulation pairs). Importantly, I observed broad subthreshold responses to many monomolecular steroid ligands (Fig. 19). These subthreshold responses were tightly coupled to the onset of chemostimulation and were reliable across repeated trials (Fig. 19). The overall envelope of depolarization was consistent with the time course of activation of MC GCaMP6f activity (Fig. 6, 7) (mean 90-10% decay time = 8.085 ± 0.0644 s, $n = 978$ cell-stimulation pairs) and previous studies (Wagner et al., 2006; Hendrickson et al., 2008; Meeks et al., 2010; Yoles-Frenkel et al., 2018).

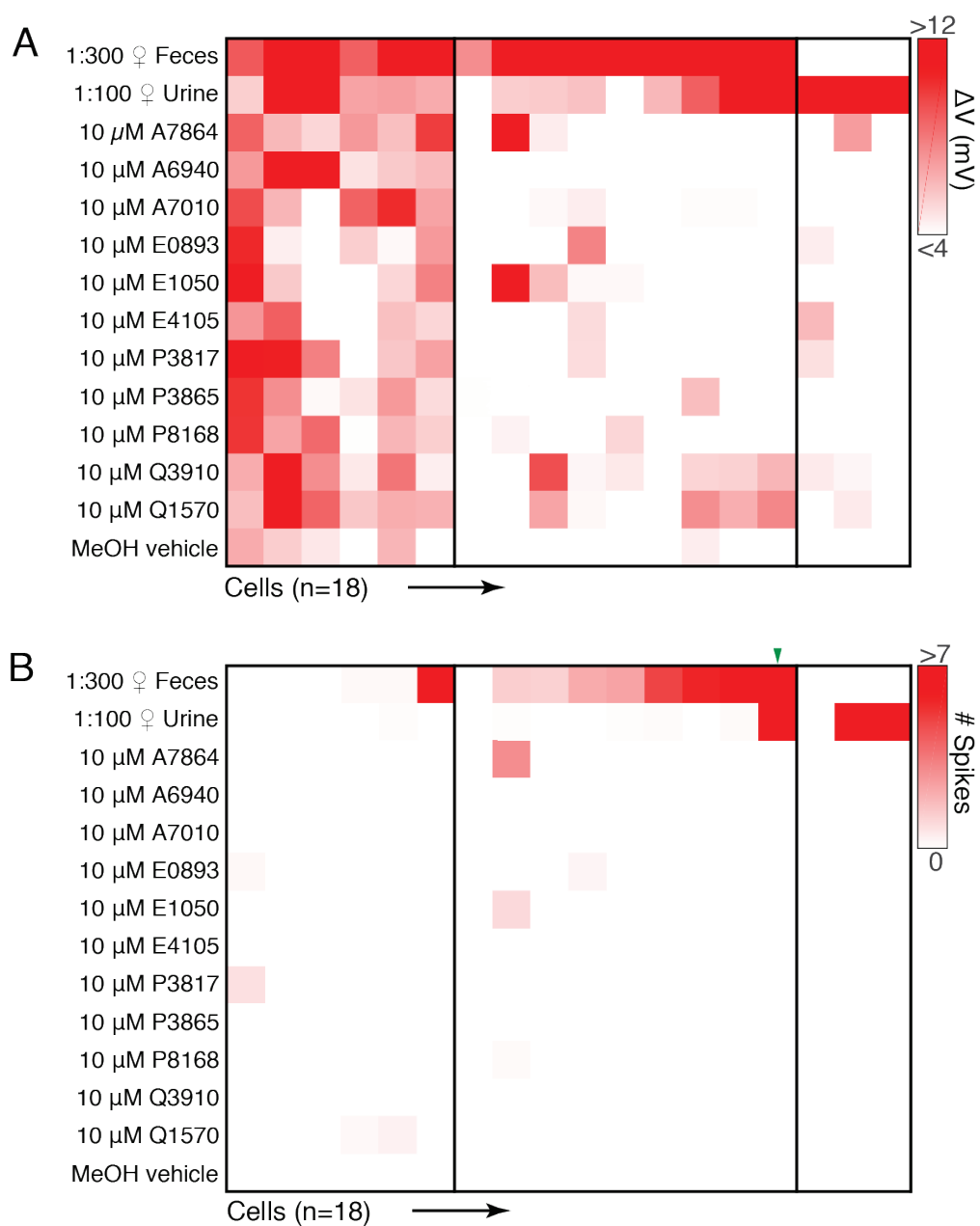


Figure 20. The heatmap summarization of 18 cells' response to the chemostimulation. (A). Heatmap of average voltage changes of 18 recorded EGCs. **(B).** Heatmap of the spiking responses of the same 18 EGCs.

Investigating the patterns of EGC subthreshold responsiveness revealed much broader MC integration than was indicated by GCaMP6f imaging experiments (Fig.

20). Out of 18 responsive EGCs, 13 showed reliable subthreshold or action potential activity evoked by monomolecular sulfated steroids (Fig. 20A, $p < 0.05$ compared to the vehicle control, Wilcoxon rank sum test). Comparing the summed sub- and suprathreshold tuning to suprathreshold-only tuning in this group of patched cells revealed the major source of discrepancy between MC and EGC tuning (Fig. 20A, B). For example, 4 of the 18 recorded cells, despite clear subthreshold responses to these stimuli, did not spike at all, and presumably would have been deemed completely unresponsive in GCaMP6f imaging experiments. Of the 14 cells that spiked in response to these stimuli, the majority (9/14) spiked only in response to naturalistic ligand blends, in agreement with GCaMP6f-based results (Fig. 11B). When I included subthreshold activation into my criteria for stimulus responsiveness, the distribution of EGC tuning was significantly right skewed (broader) than EGC distribution determined by the GCaMP6f imaging signal ($p = 2.2e-4$, Kolmogorov–Smirnov test), and became statistically indistinguishable from MCs ($p = 0.21$, Kolmogorov–Smirnov test; Fig. 21).

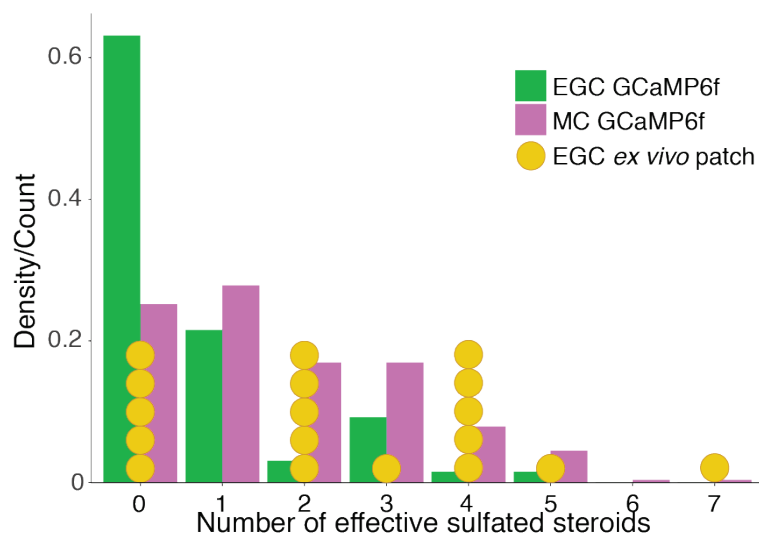


Figure 21. The distribution of MC and EGC responsiveness as revealed by Ca^{2+} imaging and *ex vivo* patch clamp.

These results help to explain my *ex vivo* Ca^{2+} imaging observations and support the hypothesis that EGCs broadly integrate from MCs (Fig. 22).

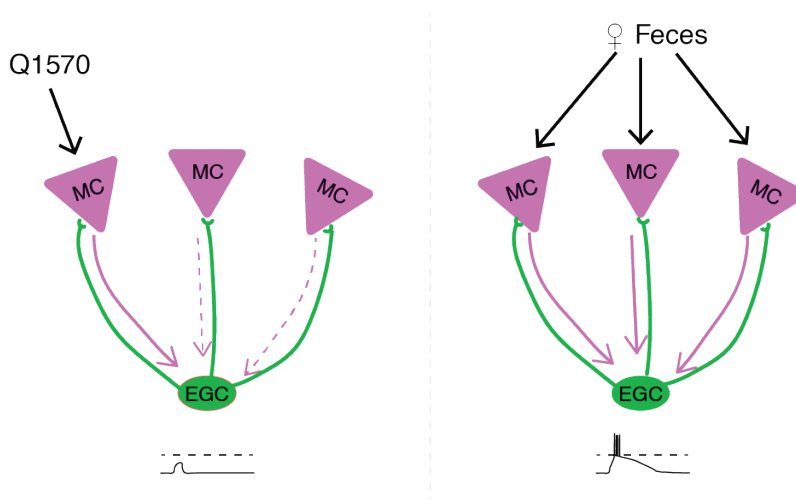


Figure 22. The integrative circuit model of EGC and MC.

However, these data also show that *Cort*⁺ EGCs are only effectively driven to spike by stimuli that collectively elicit a large fraction of AOB mitral cells (in this stimulus panel, dilute mouse urine and feces). Collectively, these results suggest that AOB EGCs perform fundamentally different roles in the AOB than PV-EPL interneurons play in the MOB. Though these cells are broad integrators, they are sparsely tuned at the level of spiking, suggesting that their activity is only stimulated in conditions in which a large ensemble of MCs is simultaneously activated.

The activation of EGCs under behavioral contexts

In the previous sections, I tried to answer the question of when and how the EGCs are recruited to fire at the level of the neural circuitry. Yet the complete answer to this question should also address the condition of EGC's activation in real-world behavioral contexts. To investigate this problem, I performed immunostaining to c-Fos, the protein product of the immediate early gene *c-fos*, after exposing the animal to the stimuli. *Cort*-Cre mice crossed with the tdTomato reporter line were used so that EGCs are marked with endogenous tdTomato. By quantifying the colocalization of c-Fos and tdTomato, the proportion of the activated EGCs is assessed.

In a pilot experiment, I investigated the effect of natural scent encounter on the EGC activation using the resident-intruder test. The resident female mouse was single-housed for 48 hours prior to the test. On the test day, the experimental female was presented 10 g bedding of adult BALB/c males (Exp, n = 1) for 45 min. The

control groups were presented either the resident's own bedding collected previously (Ctrl#1, n = 1) or fresh new bedding (Ctrl#2, n = 1).

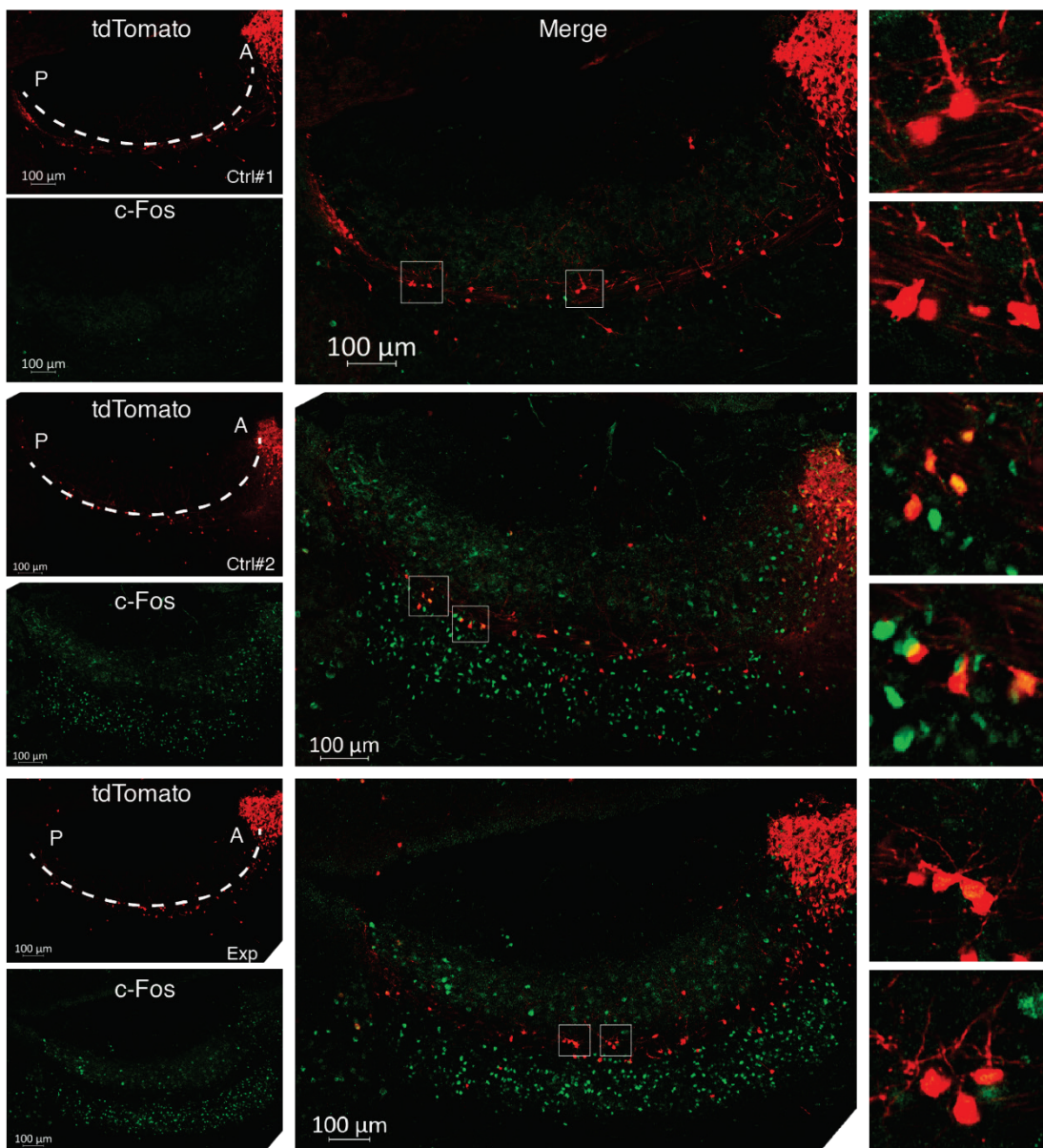


Figure 23. Immunostaining of c-Fos (green). The dashed curves mark the lateral olfactory tract (LOT). A & P represent the Anterior and Posterior respectively. Ctrl#1 is resident's own bedding; Ctrl#2 is fresh new bedding; Exp is male BALB/c bedding.

The overall AOB c-Fos level of the mouse exposed to her own bedding is significantly lower than the experimental group (Fig. 23). The c-Fos expression is concentrated at the internal cell layer. However, to my surprise, the fresh bedding also elevates the expression of c-Fos to the level comparable with the experimental group. These results suggest that the fresh bedding likely contains certain cues that would activate the AOS. Most of the AOB cells marked by the tdTomato sparsely distribute in the ECL along the LOT. These cells have visible lateral and apical dendrites, matching the morphological features of the EGC. Comparable proportion of these cells were c-Fos positive in Exp (69 of 304, 22.7%) and Ctrl#2 (29 of 127, 22.8%) (Fig. 24).

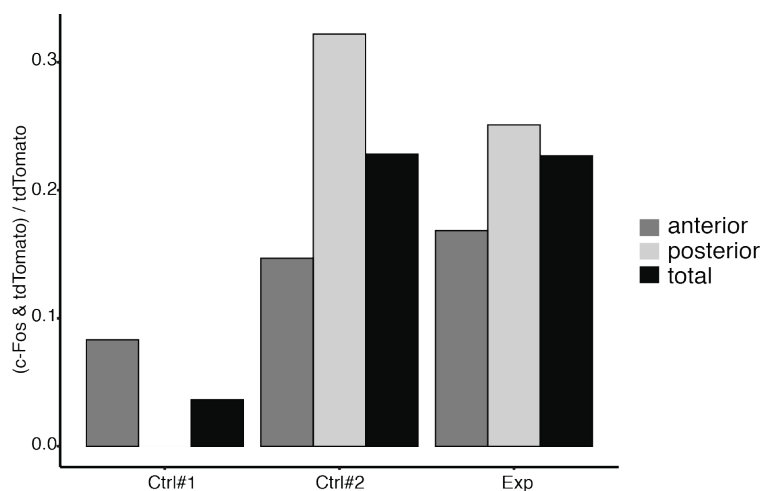


Figure 24. Percentage of c-Fos+ cells in the AOB tdTomato+ cells.

Interestingly, the Ctrl#2 also displays higher percentage of c-Fos positive neurons than the experiment groups. This result appears to be contradictory to the fact that the posterior AOB MCs receive inputs from V2R neurons, which mainly

detect protein and peptides, ligands not supposed to exist in the fresh new bedding. This could be explained by pollution of the fresh new bedding, or the validity of using c-Fos as the indicator of the neuron's recent activity.

Next, I investigated the effect of social interaction (Fig. 25). The male mice were single housed for two days prior the experiment. On the experiment day, the male mice were subject to different social stimulations. In the experiment groups, the male animals were placed into the home cage of a BALB/c female mouse. The male was allowed to interact with either a constrained BALB/c female (Exp#1, n = 1) or a freely moving BALB/c female (Exp#2, n = 1) for 75 min. The control male mouse was placed in a fresh new cage.

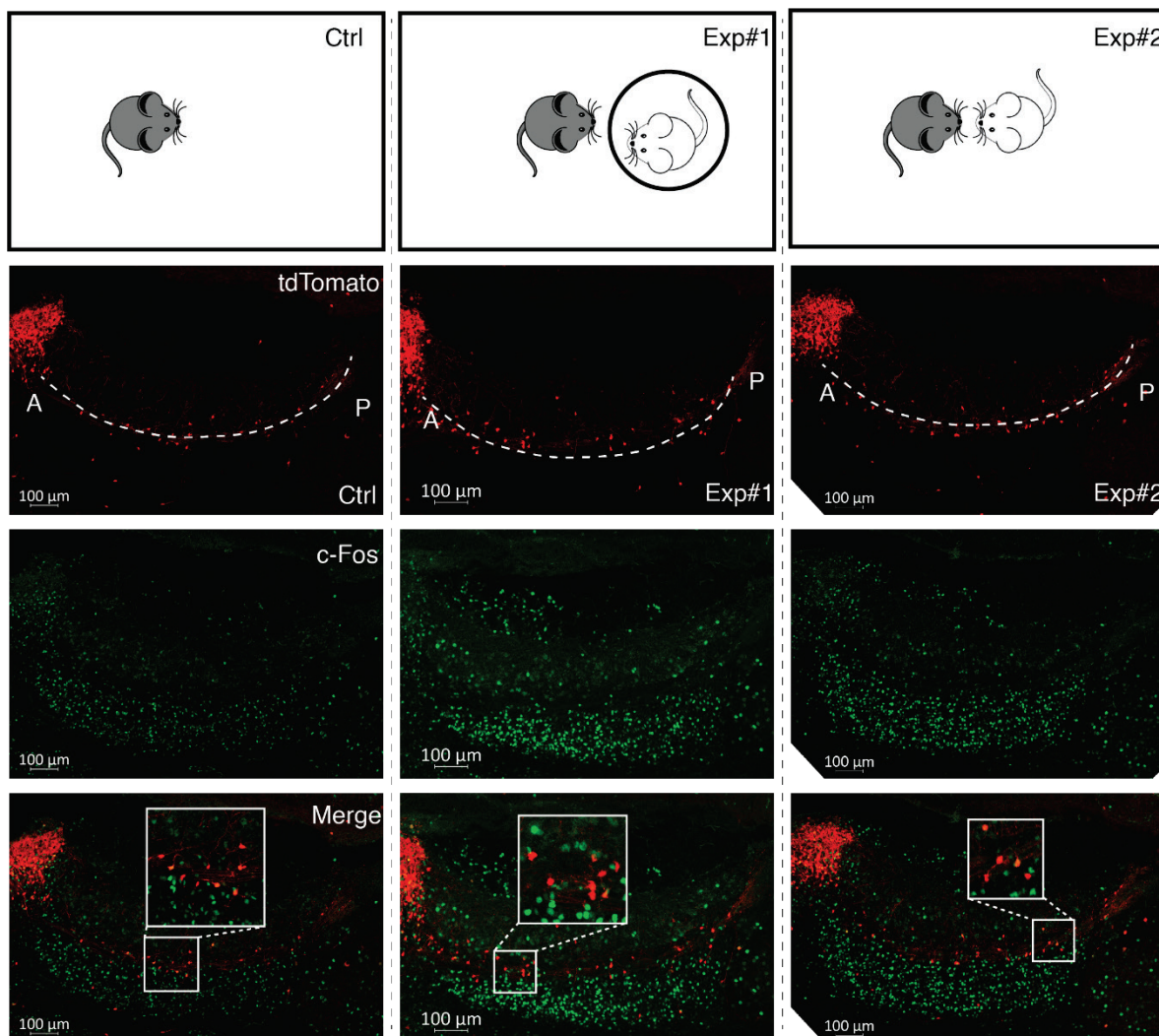


Figure 25. Immunostaining of c-Fos (green). The dashed curves mark the lateral olfactory tract (LOT). A & P represent the Anterior and Posterior respectively. Ctrl#1 is fresh new cage; Exp#1 is interacting with restrained BALB/c female; Exp#2 is freely interacting with BALB/c female.

c-Fos staining is concentrated in the ICL in all 3 groups. Not surprisingly, the control group in this experiment also displays a considerable level of c-Fos expression, but both experimental groups manifest much higher c-Fos level. Noticeably, in both Ctrl and Exp#1, the c-Fos staining seemingly biases towards the

anterior ICL whereas the Exp#2 has a uniformly high staining level in posterior ICL as well. This could be explained by that free interaction allows the male to be exposed to more chemical cues. It is also possible that extra physical interactions, such as attempts to mount, promotes the engagement of these cells.

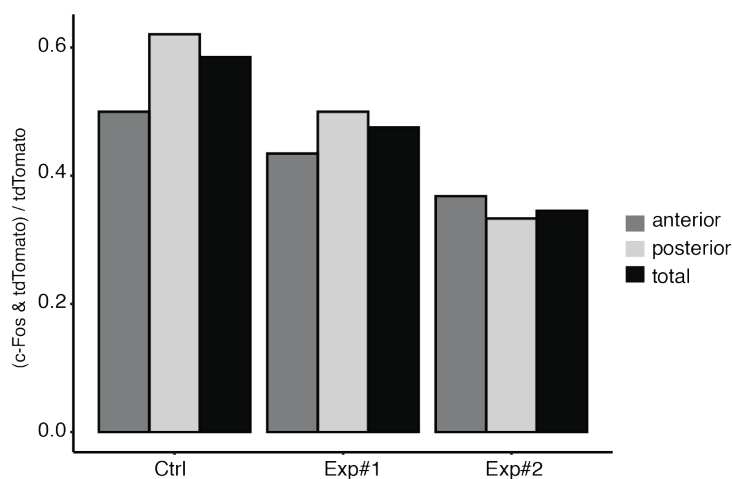


Figure 26. Percentage of c-Fos+ cells in the AOB tdTomato+ cells.

Nonetheless, such difference is not reflected in the tdTomato+ cells (Fig. 26). The percentage of c-Fos+ cells in Ctrl is even higher than that of the two experimental groups in this experiment. Although the difference can be explained by individual variance, this result is particularly intriguing with the premise that the c-Fos level in the ICL suggests a lower engagement of the AOS in the Ctrl group. This seemingly contradictory result may suggest that the EGCs are not as strongly reflecting the behavioral context as the IGCs.

Next, I probed whether directly applying the selected ligands activates the EGCs. The mice were subjected to intranasal stimuli feed. They were allowed to

freely move in their home cage for one hour before being perfused and fixed. Again, c-Fos was used as the marker for the activated neurons. *Ex vivo* recordings have revealed that naturalistic blends are strong stimulations and Q1570 is a relatively potent monomolecular ligand. Hence, for the experimental groups I applied either undiluted female BALB/c fecal extract (Exp#1, 20 μ L) or Q1570 (Exp#2, 100 mM in VNO Ringer's solution, 25 μ L). VNO Ringer's solution (30 μ L) was used in the control group. Because of the special ligand intake mechanism of the VNO, the intranasal administration was not consistent across trials. Mice handling in this process also potentially introduced certain impactful factors. Consequently, the c-Fos staining results showed large individual variation (data not shown).

CHAPTER FOUR

Conclusions and Recommendations

Cell type-specific functional studies in the AOB *ex vivo* preparation

Our knowledge of interneuron function in the AOB is generally lacking due to persistent technical challenges in recording from these neurons during VNO stimulation. For example, the AOB's precarious position beneath the rhinal sinus and opposed to the prefrontal cortex creates a physical barrier for direct access to AOB neurons. The *ex vivo* preparation of the early mouse AOB, which allows optical access to the AOB while preserving VNO-AOB functional connectivity, overcomes some of the major hurdles to performing cell type-specific investigations of chemosensory tuning. The results of *ex vivo* studies do come with their own limitations. For example, the *ex vivo* preparation eliminates the influence of potential feedback neuromodulation from downstream brain areas, which is clearly important for AOB circuit function (Oboti et al., 2018). Despite this significant limitation, by removing some *in vivo* complexities, the *ex vivo* approach has clear advantages for dissecting the basic structure and function of the AOB circuit.

By combining *ex vivo* methods with 2-photon microscopy and genetic tools for cell-type specific manipulation in the nervous system, I was able to perform the first studies of chemosensory tuning in genetically-defined AOB interneuron subsets. The specific cell types explored in this study, namely MCs, JGCs, and EGCs, represent 3 of the 4 major neuronal classes (with the remaining major class being the internal granule cells, or IGCs). These studies allowed us to produce quantitative

comparisons of each cell type's stimulus-response characteristics, and to do so across multiple randomized stimulus trials to reduce the possible impact of spontaneous activity (Holy et al., 2000; Nodari et al., 2008; Meeks et al., 2010). The utility of this combination of techniques for studying AOB circuit function is thus clear, and the results of these experiments allowed me to reveal key differences in the function of AOB EGCs compared to superficially-similar PV-EPL interneurons in the MOB (Kato et al., 2013; Miyamichi et al., 2013).

AOB EGCs are broadly innervated, but sparsely tuned to chemosensory stimuli

AOB MCs are capable of integrating excitatory input from VSNs that express different sensory vomeronasal receptors (Wagner et al., 2006) and are differentially tuned to sensory input (Meeks et al., 2010). As such, observing a high amount of tuning diversity in MCs to both naturalistic stimulation and a well-characterized panel of monomolecular sulfated steroids (Fig. 7) was expected. The specific patterns of integration by MCs adds to a growing list of studies indicating that these cells support the encoding of the identity of a chemosignal-emitting animal (Luo et al., 2003; Hendrickson et al., 2008; Ben-Shaul et al., 2010; Tolokh et al., 2013). The high degree of activation of MCs by the monomolecular sulfated steroid ligands in this panel also further supports the notion that these cells possess higher coding robustness than their VSN inputs, a feature shared by principal neurons in other

sensory circuits and species (Bhandawat et al., 2007; Meeks et al., 2010; Zhu et al., 2013).

My *a priori* hypothesis was that AOB EGCs were functionally analogous to MOB PV-EPL interneurons, so I was surprised to observe significantly sparser chemosensory tuning in EGCs compared to their upstream MCs inputs. While many EGCs were reliably activated by female BALB/c mouse urine or fecal extracts, few showed responsiveness to monomolecular ligands (Fig. 11). This result was counterintuitive, given that EGCs have extensive spinous dendritic arborizations in the ECL and receive a constant barrage of strong glutamatergic excitation from MCs, even in the absence of VSN activation (Maksimova et al., 2019). Ca^{2+} indicators, being a secondary reporter of the cells' electrophysiological activities, have drawn broad attention on their efficacy, reliability and methodologies of retrieving activities from the optical data (Huang et al., 2019; Ledochowitsch et al., 2019; Wei et al., 2019). Therefore, it is necessary to validate the possibility that performance difference would account for the sparseness. I delineated a comprehensive picture of GCaMP6f performance using whole-cell patch clamp recording and loose-seal cell-attached recording. Whole-cell patch clamp did reveal certain subtle differences. Voltage-clamp depolarization tests revealed that EGCs' GCaMP6f signals had much slower dynamics, and lower peak intensities (Fig. 13, 14), presumably because of the smaller soma size and higher input resistance of EGCs (Maksimova et al., 2019). Current-clamp current injection test is a standard procedure in benchmarking Ca^{2+} indicators (Chen et al., 2013; Inoue et al., 2019).

The slower fluorescence dynamics persisted in EGCs (Fig. 16), but the peak fluorescence change was around the similar level (EGC: 3.27 ± 0.69 , $n = 6$; MC: 3.65 ± 0.26 , $n = 4$). The physiological mechanisms underlying differential GCaMP6f signaling can be difficult to experimentally pinpoint, but may include variable expression of cytosolic Ca^{2+} buffers (Schwaller, 2010), presence or absence of somatic Ca^{2+} -permeant ion channels or differential activation of calcium-induced Ca^{2+} release from intracellular stores (Verkhratsky and Shmigol, 1996). GCaMP6f performance could vary with physiological conditions. In the whole-cell patch clamp configuration, the dialysis of intracellular medium and direct artificial current injection introduced unwanted factors. Loose-seal cell-attached recording with local field stimulation at the glomerular layer to mimic the excitatory should provide a more ideal reference. I recorded clear fluorescence signal evoked by single action potential in both EGCs and MCs (Fig. 17). A comparison of spike- $\Delta F/F$ relationships showed that EGC-GCaMP6f performed at least equally well (Fig. 18). It is worth mentioning that due to the nature of local field stimulation, the timing is less well controlled in this experiment. Nonetheless, these results suggest that EGCs and MCs do differ in GCaMP6f performance in certain contexts, but the difference is too trivial to explain the tuning differences. Regardless of the mechanisms underlying this phenomenon, these results provide important insights into the use of GCaMP6f as an activity reporter in AOB EGCs.

The differential GCaMP6f performance in EGCs and MCs is apparently not sufficient to account for EGCs' sparseness. EGCs were previously noted and

confirmed in this study for having extremely hyperpolarized resting membrane potentials (Maksimova et al., 2019), which suggested that EGCs may possess very high thresholds for action potential generation from resting states. Whole-cell patch clamp studies of EGCs in the *ex vivo* preparation revealed that, despite using the same internal and external solutions as in slice experiments, EGC resting membrane potentials were more depolarized in the *ex vivo* preparation than in slices. This could be the result of incomplete perfusion of the relatively low $[K^+]_o$ in the aCSF (2.5 mM), or perhaps due to an overall higher excitatory tone in this preparation (or both). Importantly, these resting membrane potential measurements were made in the same conditions in which EGC GCaMP6f chemosensory tuning measurements were made, suggesting that EGC resting hyperpolarization has a less dramatic impact on tuning sparseness than expected based on slice results. In these *ex vivo* whole-cell recordings, I measured chemosensory tuning responses and observed rich subthreshold sulfated steroid-evoked activity, but little spiking except in response to stimulation with urine or feces (Fig. 19, 20). Thus, despite mildly depolarized resting membrane potentials in the *ex vivo* preparation, EGCs demonstrate resistance to action potential generation unless a very large MC ensemble is simultaneously active (as is the case when the VNO is stimulated with mouse urine and feces). The broad subthreshold inputs indicate a broad connectivity, but we still lack the direct assessment of the relationship between the innervation broadness and the extent of the dendritic arbor. These two are inversely correlated in cortical PV interneurons (Runyan and Sur, 2013). The high firing threshold of the EGC could be the result of

weakness of the synaptic inputs from individual MC channel and its special intrinsic properties. Physiological mechanisms that could contribute could include selective expression of leak channels on EGC dendrites and shunting inhibition by other interneurons (Chamberland and Topolnik, 2012). Future studies will be needed to investigate the source of high EGC spiking thresholds.

It is worth also noting that although the *Cort*-T2A-Cre transgenic mice used in these studies selectively labels AOB EGCs, the *Cort*+ EGC population likely represents a fraction of the total EGC population (Maksimova et al., 2019). As such, it is possible that the chemosensory tuning I observed represents a specific subgroup of *Cort*+ EGCs. This seems unlikely, given that no differences were found between EGC morphologies, intrinsic, and synaptic features across several transgenic lines that label these cells (Maksimova et al., 2019). Also, even though *Cort*+ EGC labeling spans the anterior AOB (sensitive to sulfated steroids and many urinary and fecal cues) and posterior AOB (sensitive to urinary proteins and exocrine gland-secreted peptides), my optical recordings were largely confined to portions of the anterior AOB where responsiveness to the cues in my panel is most prominent (Meeks et al., 2010; Doyle et al., 2014). As such, it may be the case that EGCs in the posterior AOB have different tuning qualities than are indicated in this study.

Another issue worthy of addressing is the stimulation. Mice have ~300 VRs. The panel of 11 monomolecular ligands in this study, all sulfated steroids, only covers a small restricted portion of the entire ligand space. Therefore, my dataset likely has a limited coverage as well. In my analysis, only cells that are activated by

at least one of the stimuli were counted. These factors potentially lead to a bias towards the subpopulation that is either restricted to the sulfated steroids or simply more excitable in general. This system bias is unavoidable with the current experimental design. Importantly, it does not weaken the main conclusion that EGCs are much more sparsely tuned than MCs. However, a future panoramic study with a larger stimulation panel consisting of ligands from different chemical families could possibly reveal certain chemical-family-specific properties of the EGC.

Implications for models of AOB information processing

The complex physiological properties of EGCs and their chemosensory tuning are becoming clearer, but the impacts of EGC activation on MC function remain unclear. Many EGCs are labeled in *Gad2-IRES-Cre* transgenic lines (Maksimova et al., 2019), consistent with a GABAergic phenotype. EGCs are axonless and have spinous dendrites that closely appose MC dendrites, and AOB MCs are known to form reciprocal dendro-dendritic synapses with other AOB interneurons (Jia et al., 1999; Taniguchi and Kaba, 2001; Castro et al., 2007; Larriva-Sahd, 2008). Seemingly analogous PV-EPL interneurons in the MOB have been shown to be broadly inhibitory (Kato et al., 2013; Miyamichi et al., 2013). All of these pieces of evidence point to a reciprocal inhibitory function for EGCs, and future studies will be able to further elucidate EGCs' impact on MC function and information flow through the AOB.

Regardless of the specific mechanisms underlying EGCs' specific chemosensory tuning features, the observation that EGCs rarely spike in the absence of a naturalistic ligand blend has important implications for AOB circuit function. First, these results suggest that EGCs have unique roles in AOB processing that are different from PV-EPL interneurons in MOB. Despite their superficially similar circuit architectures, seemingly analogous neural types in the MOB and AOB have repeatedly been shown to have fundamentally different physiological properties (Shipley and Adamek, 1984; Jia et al., 1999; Araneda and Firestein, 2006; Wagner et al., 2006; Castro et al., 2007; Smith et al., 2015). In the MOB, PV-EPL interneurons are activated by many monomolecular odorants with low thresholds, resulting in chemosensory tuning that is close to a simple linear addition of input MCs' tuning maps (Kato et al., 2013). This quality benefits unbiased monitoring of MC activity and supports divisive normalization of MCs based on the overall population response (Kato et al., 2013; Miyamichi et al., 2013). In contrast, AOB EGCs appear to have extremely high effective thresholds despite receiving synaptic input from many MCs, which may strongly bias their activity away from monomolecular ligands and towards the blends of ligands found in natural excretions (Nodari et al., 2008). Because natural vomeronasal social cues are only known to exist in the form of such complex blends, this sparseness difference between AOB EGCs and MOB PV-EPL interneurons and AOB EGCs might reflect macroscopic differences in the natural statistics of ligand sampling between these two chemosensory pathways. It may also be the case that MC inhibition by EGCs takes

place locally at reciprocal dendrodendritic synapses independent of somatic action potentials, as has been observed in the MOB (Isaacson and Strowbridge, 1998; Schoppa et al., 1998; Chen et al., 2000; Halabisky et al., 2000; Isaacson, 2001; Egger et al., 2005; Huang et al., 2013; Bywalez et al., 2015; Lage-Rupprecht et al., 2018). It would be interesting to investigate this possibility using dendritic Ca^{2+} or voltage imaging. AOB EGCs thus appear to be, at a minimum, operating in a manner that is strikingly different than PV-EPL interneurons in the MOB, and tend not to be strongly active in the absence of broad AOB activation, raising questions about their *in vivo* roles in sensory processing. Several studies have reported individual vomeronasal ligands capable of evoking significant behavioral effects through the AOS (Chamero et al., 2007; Haga et al., 2010; Papes et al., 2010). If my results hold for the ligands that drive these behaviors, it seems unlikely that these particular chemosensory exposures engage EGCs, which may have important implications for information flow through the AOB towards its downstream targets in the limbic system (Martinez-Marcos, 2009; Gutiérrez-Castellanos et al., 2014; Stowers and Liberles, 2016).

An interesting perspective comes from placing EGCs in a big picture of inhibitory interneurons. Canonically, inhibitory interneurons are thought to be more broadly tuned than the principal cells, as have been observed in multiple sensory areas (Sohya et al., 2007; Niell and Stryker, 2008; Kato et al., 2013; Znamenskiy et al., 2018). The broadness is attributed to the dense connection between a relatively small number of inhibitory interneurons and a large number of principal cells (Hofer

et al., 2011; Packer and Yuste, 2011; Miyamichi et al., 2013). However, several studies challenged this view by showing that inhibitory interneurons in certain cases have the similar encoding capacity as the principal cells (Moore and Wehr, 2013; Gritton et al., 2019; Najafi et al., 2019), suggesting a diversity of connection patterns. Apparently, EGCs are different from the broadly tuned inhibitory interneurons, and their encoding space is not as capacious as the MCs either. They might represent a unique category that directly implements logic computations such as the AND gate.

In sum, these experiments contribute a wealth of information about chemosensory tuning of specific AOB cell types, adding important quantitative constraints on the role of inhibitory interneurons on AOB circuit function.

Other questions and future directions

My experimental results suggest that EGCs bias to the natural blends of the stimulation. A natural conjecture is that it might respond to an artificial blend of multiple ligands more strongly than to a singular ligand stimulus with same concentration. In other words, the integrative inputs make EGCs more sensitive to the variety of ligands than to the concentration. During my experiments, I pilot-tested a mixture of all steroids at 4 μM individually, hence 44 μM sulfated steroid in total. In GCaMP6f imaging experiments, all mixture responsive EGCs responded to at least one of the 10 μM steroids. In *ex vivo* patch clamp recordings, I did not observe any superlinear summation either (data not shown). Future scrutiny on this question requires a more carefully designed stimulation formula. The stimulation

concentration should be controlled to avoid evoking non-specific activities, and ligands outside of the steroid family should be included in the blends.

Another important question not touched in this research is the model of the inhibition imposed by the EGCs. My initial hypothesis was that EGCs impose divisive inhibition onto the MCs via their reciprocal synapses, resembling the EPL-PV neurons in the MOB. However, because EGC tuning profile displayed substantial disparity to the EPL-PV neurons, their functional role in the AOB circuit remains open to other possibilities. To probe this aspect, one needs to record MCs while manipulating EGC activities. Given the exceptionally sparse firing of EGCs, a promising direction would be to measure the activated EGCs' impact on MCs. The insights about the circuitry functions of EGCs could be a stepstone for linking them with the animal behavior. However, because local inhibitory interneurons usually are not directly involved in information encoding and projection, this goal could be challenging. The functional role of EGCs can be highly situational. In my pilot studies (Fig. 23, 25), the activation of EGCs as indicated by the expression of the immediate early gene c-Fos did not show as clear selectivity towards the behavioral contexts as the IGCs. The other major drawback is that our experiment design is currently limited by the lack of reliable fast-readout paradigms for complicate AOB-dependent animal behaviors. These behaviors include immediate or 'releaser' responses and the long-lasting 'primer' responses that could require largely different testing strategies (Dulac and Torello, 2003). The test of the mating memory using the pregnancy block effect is robust (Lloyd-Thomas and Keverne, 1982; Matsuoka et al.,

2004), but this test only covers one of the many social behaviors that the AOS governs. I expect that an experiment as simple and versatile as the place preference test would facilitate our investigation on this problem (Becker and Hurst, 2009).

Another interesting question is the plasticity of EGC-MC connection. Synaptic plasticity has been proven to be the key to the neural computation and information storage in classic studies of hippocampus, cerebellum and many other brain areas. In the closely related MOB, the plasticity of granule cells has been shown important for olfactory discrimination and olfactory learning by myriad studies (Abraham et al., 2010; Livneh and Mizrahi, 2012; Moreno et al., 2012; Gschwend et al., 2015; Huang et al., 2016). The AOB was shown to be responsible for the formation and maintenance of mouse mating memory. The prevailing model attributes the formation of mating memory to the MC-interneuron plasticity (Brennan, 2009). Existing studies have revealed the importance of GABAergic transmission in the Bruce effect (pregnancy block) (Brennan et al., 1995; Brennan and Binns, 2005). Indeed, the remodeling of AOB reciprocal synapses after long-term mating memory formation has been reported previously (Matsuoka et al., 2004). Recent scrutiny revealed the change of intrinsic properties of AOB IGCs after social encounter (Cansler et al., 2017). Although, to my knowledge, no direct observations regarding to the EGC contextual plasticity have been reported, it is possible that certain social contexts might change the strength of EGC-MC synaptic connections, or the intrinsic properties of EGCs and result an altered tuning integration outcome in EGCs. EGCs' high threshold cutoff could be a gating mechanism that only allows the naturalistic

information-carrying stimuli such as urine, feces and other odorant-rich animal secretions to trigger the circuitry remodeling, hence improves the system's noise robustness. A potential experiment to verify this hypothesis is to measure the responsivity of EGCs of female mice after mating. I expect behavioral contexts like mating would give rise to potentiated MC-EGC communication, and significantly change the tuning profile of EGCs. If this is true, then a comparison between EGCs' responsivity to the mating partner and that to a stranger male, should reveal interesting insights about the neuronal mechanisms of the AOB-dependent mating memory (Fig. 27).

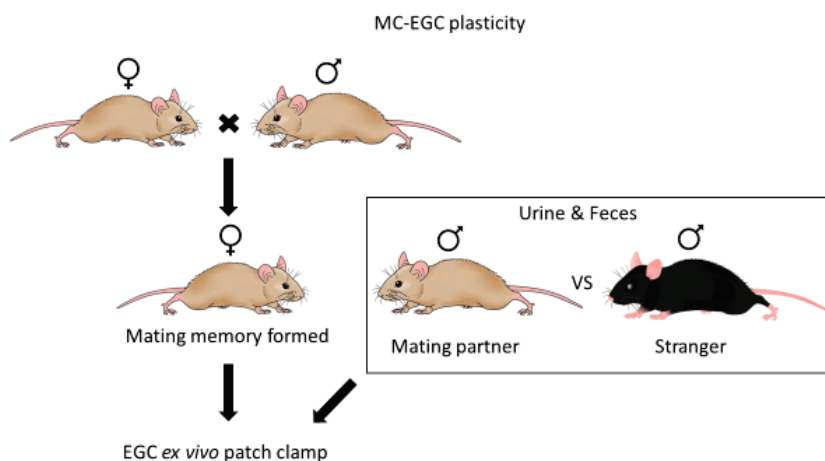


Figure 27. Measure EGCs' responsivity after mating.

The roles of various neuromodulators in regulating EGC activities are important too. The MOB granule cells are state-dependent (Kato et al., 2012; Cazakoff et al., 2014), strongly affected by the noradrenaline (NA) (Moreno et al., 2012). NA is also

considered as an important part of the AOB plasticity because its surge was observed upon the formation of mating memory (Brennan et al., 1995) and was considered to reduce the GABA transmission and facilitate metabotropic glutamate receptor (mGluR) activation. Though NA has been shown to be important for the mating memory formation (Rosser and Keverne, 1985; Kaba and Keverne, 1988), its function in modulating circuitry signal was shown to be heterogenous (Doyle and Meeks, 2017). Additionally, oxytocin was also reported to be part of the AOB plasticity (Fang et al., 2008). Testing the modulatory effect of these neuromodulators as well as other unreported ones would be necessary to obtain a full picture of EGCs.

The developmental traces of EGCs as well as other AOB interneurons are not completely clear. Like the granule cells in the MOB, the AOB interneurons are also constantly functionally replenished by the adult-born neurons (Peretto et al., 2001; Nunez-Parra et al., 2011). The mature and immature MOB granule cells could have distinct tuning broadness and have different contributions to the olfactory discrimination (Quast et al., 2017; Li et al., 2018; Alonso et al., 2019). The maturation and the connectivity are also experience-dependent (Livneh and Mizrahi, 2012; Moreno et al., 2012; Sailor et al., 2016; Quast et al., 2017; Mandairon et al., 2018; Forest et al., 2019). Likewise, the adult neurogenesis of AOB granule cells is also regulated by the experience (Nunez-Parra et al., 2011). I did not address the maturity of the EGCs in this study, but it is possible that mature and immature EGCs can also be functionally distinguished.

Concluding remarks

Here I described the first targeted study of one major AOB inhibitory interneuron subtype, EGC. Experimental results showed that EGCs paradoxically are much narrowly tuned than MCs, apparently contradictory to their broad synaptic connections. Patch clamp recordings revealed broadly innervated subthreshold activities in EGCs, suggesting that the sparseness is caused by the high threshold of somatic firing. I proposed that this discovery suggests a different information processing logic of the AOB EGC-MC circuit, relative to the MOB PV-MC circuit, particularly suiting the processing of pheromones which are often found in body fluids with complex composition. This pioneering study revealed important insights of AOB EGCs, and also raised more key questions for future researchers. What is the modulatory function of EGCs on the AOB circuit? Do they contribute to the AOB-dependent animal behaviors such as the formation of mating memory? Answering these questions would help us understand the AOB's role in guiding mouse social behaviors.

BIBLIOGRAPHY

- Abraham NM, Egger V, Shimshek DR, Renden R, Fukunaga I, Sprengel R, Seeburg PH, Klugmann M, Margrie TW, Schaefer AT, Kuner T (2010) Synaptic Inhibition in the Olfactory Bulb Accelerates Odor Discrimination in Mice. *Neuron*:399-411.
- Alonso S, Reinert JK, Marichal N, Massalini S, Berninger B, Kuner T, Calegari F (2019) An increase in neural stem cells and olfactory bulb adult neurogenesis improves discrimination of highly similar odorants. *The EMBO Journal*.
- Araneda RC, Firestein S (2006) Adrenergic Enhancement of Inhibitory Transmission in the Accessory Olfactory Bulb. *The Journal of Neuroscience* 26:3292-3298.
- Becker SD, Hurst JL (2009) Female behaviour plays a critical role in controlling murine pregnancy block. *Proceedings of the Royal Society of London B: Biological Sciences* 276:1723-1729.
- Ben-Shaul Y, Katz LC, Mooney R, Dulac C (2010) In vivo vomeronasal stimulation reveals sensory encoding of conspecific and allospecific cues by the mouse accessory olfactory bulb. *Proceedings of the National Academy of Sciences* 107:5172-5177.
- Berghard A, Buck LB (1996) Sensory transduction in vomeronasal neurons: evidence for G alpha o, G alpha i2, and adenylyl cyclase II as major components of a pheromone signaling cascade. *The Journal of Neuroscience* 16:909-918.
- Bhandawat V, Olsen SR, Gouwens NW, Schlieff ML, Wilson RI (2007) Sensory processing in the Drosophila antennal lobe increases reliability and separability of ensemble odor representations. *Nature Neuroscience* 10:1474-1482.
- Braganza O, Beck H (2018) The Circuit Motif as a Conceptual Tool for Multilevel Neuroscience. *Trends in Neurosciences* 41:128-136.
- Brennan PA (2001) The vomeronasal system. *Cellular and Molecular Life Sciences CMLS* 58:546-555.
- Brennan PA (2009) Outstanding issues surrounding vomeronasal mechanisms of pregnancy block and individual recognition in mice. *Behav Brain Res* 200.
- Brennan PA, Keverne EB (1997) Neural mechanisms of mammalian olfactory learning. *Progress in Neurobiology* 51:457-481.
- Brennan PA, Binns EK (2005) Vomeronasal mechanisms of mate recognition in mice. *Chemical senses*.
- Brennan PA, Kendrick KM, Neuroscience K-EB (1995) Neurotransmitter release in the accessory olfactory bulb during and after the formation of an olfactory memory in mice. *Neuroscience*.

- Bywalez WG, Patirniche D, Rupprecht V, Stemmler M, Herz A, Pálfi D, Rózsa B, Egger V (2015) Local Postsynaptic Voltage-Gated Sodium Channel Activation in Dendritic Spines of Olfactory Bulb Granule Cells. *Neuron* 85:590-601.
- Cansler HL, Maksimova MA, Meeks JP (2017) Experience-dependent plasticity in accessory olfactory bulb interneurons following male-male social interaction. *bioRxiv*:127589.
- Castro JB, Hovis KR, Urban NN (2007) Recurrent Dendrodendritic Inhibition of Accessory Olfactory Bulb Mitral Cells Requires Activation of Group I Metabotropic Glutamate Receptors. *The Journal of Neuroscience* 27:5664-5671.
- Cazakoff BN, Lau BYB, Crump KL, Demmer HS, Shea SD (2014) Broadly tuned and respiration-independent inhibition in the olfactory bulb of awake mice. *Nature Neuroscience*.
- Chamberland S, Topolnik L (2012) Inhibitory control of hippocampal inhibitory neurons. *Frontiers in Neuroscience* 6:165.
- Chamero P, Marton TF, Logan DW, Flanagan K, Cruz JR, Saghatelian A, Cravatt BF, Stowers L (2007) Identification of protein pheromones that promote aggressive behaviour. *Nature* 450:899.
- Cheetham SA, Thom MD, Jury F, Ollier W, Beynon RJ, Hurst JL (2007) The Genetic Basis of Individual-Recognition Signals in the Mouse. *Current Biology*:1771-1777.
- Chen TW, Wardill TJ, Sun Y, Pulver SR, Renninger SL, Baohan A, Schreiter ER, Kerr RA, Orger MB, Jayaraman V, Looger LL, Svoboda K, Kim DS (2013) Ultrasensitive fluorescent proteins for imaging neuronal activity. *Nature* 499:295-300.
- Chen WR, Xiong W, Shepherd GM (2000) Analysis of Relations between NMDA Receptors and GABA Release at Olfactory Bulb Reciprocal Synapses. *Neuron* 25:625-633.
- Dana H, Sun Y, Mohar B, Hulse BK, Kerlin AM, Hasseman JP, Tsegaye G, Tsang A, Wong A, Patel R, Macklin JJ, Chen Y, Konnerth A, Jayaraman V, Looger LL, Schreiter ER, Svoboda K, Kim DS (2019) High-performance calcium sensors for imaging activity in neuronal populations and microcompartments. *Nature Methods*:649-657.
- Dey S, Chamero P, Pru JK, Chien M-S, Ibarra-Soria X, Spencer KR, Logan DW, Matsunami H, Peluso JJ, Stowers L (2015) Cyclic Regulation of Sensory Perception by a Female Hormone Alters Behavior. *Cell*:1334-1344.
- Doyle WI, Meeks JP (2017) Heterogeneous effects of noradrenaline on spontaneous and stimulus-driven activity in the male accessory olfactory bulb. *Journal of neurophysiology* 117.

- Doyle WI, Hammen GF, Meeks JP (2014) Ex Vivo Preparations of the Intact Vomeronasal Organ and Accessory Olfactory Bulb. *Journal of Visualized Experiments*.
- Doyle WI, Dinser JA, Cansler HL, Zhang X, Dinh DD, Browder NS, Riddington IM, Meeks JP (2016) Faecal bile acids are natural ligands of the mouse accessory olfactory system. *Nature Communications* 7:11936.
- Dulac C, Axel R (1995) A novel family of genes encoding putative pheromone receptors in mammals. *Cell* 83:195-206.
- Dulac C, Torello TA (2003) Molecular detection of pheromone signals in mammals: from genes to behaviour. *Nature Reviews Neuroscience* 4:551-562.
- Egger V, Svoboda K, Mainen ZF (2005) Dendrodendritic Synaptic Signals in Olfactory Bulb Granule Cells: Local Spine Boost and Global Low-Threshold Spike. *The Journal of Neuroscience* 25:3521-3530.
- Fang LY, Quan RD, Kaba H (2008) Oxytocin facilitates the induction of long-term potentiation in the accessory olfactory bulb. *Neuroscience Letters*.
- Ferguson BR, Gao W-J (2018) PV Interneurons: Critical Regulators of E/I Balance for Prefrontal Cortex-Dependent Behavior and Psychiatric Disorders. *Frontiers in Neural Circuits* 12:37.
- Ferrero DM, Moeller LM, Osakada T, Horio N, Li Q, Roy DS, Cichy A, Spehr M, Touhara K, Liberles SD (2013) A juvenile mouse pheromone inhibits sexual behaviour through the vomeronasal system. *Nature* 502:368.
- Finlayson JS, Asofsky R, Potter M, Runner CC (1965) Major Urinary Protein Complex of Normal Mice: Origin. *Science*:981-982.
- Forest J, Chalençon L, Midroit M, Terrier C, Caillé I, Sacquet J, Benetollo C, Martin K, Richard M, Didier A, Mandairon N (2019) Role of Adult-Born Versus Preexisting Neurons Born at P0 in Olfactory Perception in a Complex Olfactory Environment in Mice. *Cerebral Cortex*.
- Gao Y, Budlong C, Durlacher E, Davison IG (2017) Neural mechanisms of social learning in the female mouse. *eLife* 6.
- Gorin M, Tsitoura C, Kahan A, Watznauer K, Drose DR, Arts M, Mathar R, O'Connor S, Hanganu-Opatz IL, Ben-Shaul Y, Spehr M (2016) Interdependent Conductances Drive Intraslow Intrinsic Rhythmogenesis in a Subset of Accessory Olfactory Bulb Projection Neurons. *The Journal of Neuroscience* 36:3127-3144.
- Gritton HJ, Howe WM, Romano MF, DiFeliceantonio AG, Kramer MA, Saligrama V, Bucklin ME, Zemel D, Han X (2019) Unique contributions of parvalbumin and

cholinergic interneurons in organizing striatal networks during movement. *Nature Neuroscience*:586-597.

Gschwend O, Abraham NM, Lagier S, Begnaud F (2015) Neuronal pattern separation in the olfactory bulb improves odor discrimination learning. *Nature Neuroscience*.

Guillaume O (2000) Role of chemical communication and behavioural interactions among conspecifics in the choice of shelters by the cave-dwelling salamander *Proteus anguinus* (Caudata, Proteidae). *Canadian Journal of Zoology* 78:167-173.

Gutiérrez - Castellanos N, Pardo - Bellver C, Martínez - García F, Lanuza E (2014) The vomeronasal cortex – afferent and efferent projections of the posteromedial cortical nucleus of the amygdala in mice. *European Journal of Neuroscience* 39:141-158.

Haga S, Hattori T, Sato T, Sato K, Matsuda S, Kobayakawa R, Sakano H, Yoshihara Y, Kikusui T, Touhara K (2010) The male mouse pheromone ESP1 enhances female sexual receptive behaviour through a specific vomeronasal receptor. *Nature* 466:118.

Halabisky B, Friedman D, Radojicic M, Strowbridge BW (2000) Calcium Influx through NMDA Receptors Directly Evokes GABA Release in Olfactory Bulb Granule Cells. *Journal of Neuroscience* 20:5124-5134.

Hammen GF, Turaga D, Holy TE, Meeks JP (2014) Functional organization of glomerular maps in the mouse accessory olfactory bulb. *Nat Neurosci* 17.

Häusser M, Margrie TW (2013) Two-Photon Targeted Patching and Electroporation In Vivo. *Cold Spring Harbor Protocols* 2014.

Hendrickson RC, Krauthamer S, Essenberg JM, Holy TE (2008) Inhibition shapes sex selectivity in the mouse accessory olfactory bulb. *J Neurosci* 28.

Herrada G, Dulac C (1997) A Novel Family of Putative Pheromone Receptors in Mammals with a Topographically Organized and Sexually Dimorphic Distribution. *Cell*:763-773.

Hofer SB, Ko H, Pichler B, Vogelstein J, Ros H, Zeng H, Lein E, Lesica NA, Mrsic-Flogel TD (2011) Differential connectivity and response dynamics of excitatory and inhibitory neurons in visual cortex. *Nature Neuroscience*:1045-1052.

Holy TE, Dulac C, Meister M (2000) Responses of Vomeronasal Neurons to Natural Stimuli. *Science* 289:1569-1572.

Houck LD (2009) Pheromone Communication in Amphibians and Reptiles. *Physiology*:161-176.

- Huang L, Garcia I, Jen H-II, Arenkiel BR (2013) Reciprocal connectivity between mitral cells and external plexiform layer interneurons in the mouse olfactory bulb. *Front Neural Circuits* 7.
- Huang L, Ung K, Garcia I, Quast KB, Cordiner K, Saggau P, Arenkiel BR (2016) Task learning promotes plasticity of interneuron connectivity maps in the olfactory bulb. *Journal of Neuroscience*.
- Huang L, Knoblich U, Ledochowitsch P, Lecoq J, Reid CR, de Vries SEJ, Buice MA, Murphy GJ, Waters J, Koch C, Zeng H, Li L (2019) Relationship between spiking activity and simultaneously recorded fluorescence signals in transgenic mice expressing GCaMP6. *bioRxiv:788802*.
- Hurst JL, Robertson D, Tolladay U, Beynon RJ (1998) Proteins in urine scent marks of male house mice extend the longevity of olfactory signals. *Animal Behaviour:1289-1297*.
- Inoue M et al. (2019) Rational Engineering of XCaMPs, a Multicolor GECI Suite for In Vivo Imaging of Complex Brain Circuit Dynamics. *Cell:1346*.
- Isaacson JS (2001) Mechanisms governing dendritic γ -aminobutyric acid (GABA) release in the rat olfactory bulb. *Proceedings of the National Academy of Sciences* 98:337-342.
- Isaacson JS, Strowbridge BW (1998) Olfactory Reciprocal Synapses: Dendritic Signaling in the CNS. *Neuron* 20:749-761.
- Isaacson JS, Scanziani M (2011) How Inhibition Shapes Cortical Activity. *Neuron* 72:231-243.
- Isogai Y, Si S, Pont-Lezica L, Tan T, Kapoor V, Murthy VN, Dulac C (2011) Molecular organization of vomeronasal chemoreception. *Nature* 478:241-245.
- Jacob S, McClintock MK, Zelano B, Ober C (2002) Paternally inherited HLA alleles are associated with women's choice of male odor. *Nature Genetics:175-179*.
- Jeanne JM, Wilson RI (2015) Convergence, Divergence, and Reconvergence in a Feedforward Network Improves Neural Speed and Accuracy. *Neuron* 88.
- Jia C, Goldman G, Halpern M (1997) Development of vomeronasal receptor neuron subclasses and establishment of topographic projections to the accessory olfactory bulb. *Developmental Brain Research* 102:209-216.
- Jia C, Chen WR, Shepherd GM (1999) Synaptic Organization and Neurotransmitters in the Rat Accessory Olfactory Bulb. *Journal of Neurophysiology* 81:345-355.
- Jordan WC, Bruford MW (1998) New perspectives on mate choice and the MHC. *Heredity:127-133*.

- Kaba H, Keverne EB (1988) The effect of microinfusions of drugs into the accessory olfactory bulb on the olfactory block to pregnancy. *Neuroscience*.
- Kaba H, Nakanishi S (1995) Synaptic Mechanisms of Olfactory Recognition Memory. *Rev Neuroscience* 6.
- Kaba H, Huang G-ZZ (2005) Long-term potentiation in the accessory olfactory bulb: a mechanism for olfactory learning. *Chem Senses* 30 Suppl 1.
- Karlson P, LÜScher M (1959) 'Pheromones': a New Term for a Class of Biologically Active Substances. *Nature* 183:55-56.
- Kato HK, Chu MW, Isaacson JS, Neuron K-T (2012) Dynamic sensory representations in the olfactory bulb: modulation by wakefulness and experience. *Neuron*.
- Kato HK, Gillet SN, Peters AJ, Isaacson JS, Komiyama T (2013) Parvalbumin-expressing interneurons linearly control olfactory bulb output. *Neuron* 80.
- Kepecs A, Fishell G (2014) Interneuron cell types are fit to function. *Nature* 505:318-326.
- Keverne EB, Brennan PA (1996) Olfactory recognition memory. *Journal of Physiology-Paris* 90:399-401.
- Laberge F, Hara TJ (2001) Neurobiology of fish olfaction: a review. *Brain Research Reviews*:46-59.
- Lage-Rupprecht V, Jodar T, Yeghiazaryan G, Rozsa B, Egger V (2018) Local reciprocal release of GABA from dendritic spines of olfactory bulb granule cells requires local sodium channel activation and occurs on both fast and slow timescales. *bioRxiv*:440198.
- Larriva-Sahd J (2008) The accessory olfactory bulb in the adult rat: a cytological study of its cell types, neuropil, neuronal modules, and interactions with the main olfactory system. *J Comp Neurol* 510:309-350.
- Leclaire S, Strandh M, Mardon J, Westerdahl H, Bonadonna F (2017) Odour-based discrimination of similarity at the major histocompatibility complex in birds. *Proceedings Biological sciences*:20162466.
- Ledochowitsch P, Huang L, Knoblich U, Oliver M, Lecoq J, Reid C, Li L, Zeng H, Koch C, Waters J, de Vries S, Buice MA (2019) On the correspondence of electrical and optical physiology in in vivo population-scale two-photon calcium imaging. *bioRxiv*:800102.
- Leinders-Zufall T, Lane AP, Puche AC, Ma W, Novotny MV, Shipley MT, Zufall F (2000) Ultrasensitive pheromone detection by mammalian vomeronasal neurons. *Nature* 405:792.

- Leinders-Zufall T, Brennan P, Widmayer P, S PC, Maul-Pavicic A, Jäger M, Li X-HH, Breer H, Zufall F, Boehm T (2004) MHC class I peptides as chemosensory signals in the vomeronasal organ. *Science (New York, NY)* 306:1033-1037.
- Li WL, Chu MW, Wu A, Suzuki Y, Imayoshi I, Komiyama T (2018) Adult-born neurons facilitate olfactory bulb pattern separation during task engagement. *eLife*.
- Liberles SD (2014) Mammalian Pheromones. *Physiology* 76:151-175.
- Livneh Y, Mizrahi A (2012) Experience-dependent plasticity of mature adult-born neurons. *Nature Neuroscience*:26-28.
- Lloyd-Thomas A, Keverne EB (1982) Role of the brain and accessory olfactory system in the block to pregnancy in mice. *Neuroscience*.
- Luo M, Fee MS, Katz LC (2003) Encoding Pheromonal Signals in the Accessory Olfactory Bulb of Behaving Mice. *Science* 299:1196-1201.
- Madisen L, Zwingman TA, Sunkin SM, Oh SW, Zariwala HA, Gu H, Ng LL, Palmiter RD, Hawrylycz MJ, Jones AR, Lein ES, Zeng H (2010) A robust and high-throughput Cre reporting and characterization system for the whole mouse brain. *Nature neuroscience* 13:133-140.
- Maksimova MA, Cansler HL, Zuk KE, Torres JM, Roberts DJ, Meeks JP (2019) Interneuron functional diversity in the mouse accessory olfactory bulb. *bioRxiv*:552463.
- Mandairon N, Kuczewski N, Kermen F, Forest J, Midroit M, Richard M, Thevenet M, Sacquet J, Linster C, Didier A (2018) Opposite regulation of inhibition by adult-born granule cells during implicit versus explicit olfactory learning. *eLife*.
- Martinez-Marcos A (2009) On the organization of olfactory and vomeronasal cortices. *Progress in Neurobiology* 87:21-30.
- Matsunami H, Buck LB (1997) A multigene family encoding a diverse array of putative pheromone receptors in mammals. *Cell* 90:775-784.
- Matsuoka M, Kaba H, of ... M-K (2004) Remodeling of reciprocal synapses associated with persistence of long - term memory. *European Journal of ...*
- Matsuoka M, Kaba H, Mori Y, Neuroreport I-M (1997) Synaptic plasticity in olfactory memory formation in female mice. *Neuroreport*.
- McElfresh SJ, Millar JG (2001) Geographic variation in the pheromone system of the saturniid moth *hemileuca eglanterina*. *Ecology* 82:3505-3518.
- Meeks JP, Holy TE (2009) An ex vivo preparation of the intact mouse vomeronasal organ and accessory olfactory bulb. *Journal of Neuroscience Methods* 177:440-447.

- Meeks JP, Arnson HA, Holy TE (2010) Representation and transformation of sensory information in the mouse accessory olfactory system. *Nature neuroscience*.
- Meredith M, O'Connell RJ (1979) Efferent control of stimulus access to the hamster vomeronasal organ. *The Journal of Physiology*:301-316.
- Miyamichi K, Shlomai-Fuchs Y, Shu M, Weissbourd BC, Luo L, Mizrahi A (2013) Dissecting local circuits: parvalbumin interneurons underlie broad feedback control of olfactory bulb output. *Neuron* 80.
- Mohrhardt J, Nagel M, Fleck D, Ben-Shaul Y, Spehr M (2018) Signal Detection and Coding in the Accessory Olfactory System. *Chemical Senses* 43:667-695.
- Moore AK, Wehr M (2013) Parvalbumin-Expressing Inhibitory Interneurons in Auditory Cortex Are Well-Tuned for Frequency. *The Journal of Neuroscience*:13713-13723.
- Moreno MM, Bath K, of ... K-N (2012) Action of the noradrenergic system on adult-born cells is required for olfactory learning in mice. *Journal of ...*
- Moriya-Ito K, Endoh K, Fujiwara-Tsukamoto Y, Ichikawa M (2013) Three-dimensional reconstruction of electron micrographs reveals intrabulbar circuit differences between accessory and main olfactory bulbs. *Frontiers in Neuroanatomy* 7:5.
- Nagai Y, Sano H, Yokoi M (2005) Transgenic expression of Cre recombinase in mitral/tufted cells of the olfactory bulb. *genesis* 43:12-16.
- Nagayama S, Homma R, Imamura F (2014) Neuronal organization of olfactory bulb circuits. *Frontiers in Neural Circuits* 8.
- Najafi F, Elsayed GF, Cao R, Pnevmatikakis E, Latham PE, Cunningham JP, Churchland AK (2019) Excitatory and Inhibitory Subnetworks Are Equally Selective during Decision-Making and Emerge Simultaneously during Learning. *Neuron*:165-720130816.
- Niell CM, Stryker MP (2008) Highly Selective Receptive Fields in Mouse Visual Cortex. *The Journal of Neuroscience*:7520-7536.
- Nodari F, Hsu F-F, Fu X, Holekamp TF, Kao L-F, Turk J, Holy TE (2008) Sulfated Steroids as Natural Ligands of Mouse Pheromone-Sensing Neurons. *The Journal of Neuroscience* 28:6407-6418.
- Nunez-Parra A, Pugh V, Araneda RC (2011) Regulation of adult neurogenesis by behavior and age in the accessory olfactory bulb. *Molecular and Cellular Neuroscience*:274-285.

Oboti L, Russo E, Tran T, Durstewitz D, Corbin JG (2018) Amygdala Corticofugal Input Shapes Mitral Cell Responses in the Accessory Olfactory Bulb. *eNeuro* 5:18.

Packer AM, Yuste R (2011) Dense, Unspecific Connectivity of Neocortical Parvalbumin-Positive Interneurons: A Canonical Microcircuit for Inhibition? *The Journal of Neuroscience*:13260-13271.

Papes F, Logan DW, Stowers L (2010) The Vomeronasal Organ Mediates Interspecies Defensive Behaviors through Detection of Protein Pheromone Homologs. *Cell* 141:692-703.

Penn D, Potts WK (1998) Untrained mice discriminate MHC-determined odors. *Physiology & Behavior*:235-243.

Peretto P, Giachino C, Panzica G, Fasolo A (2001) Sexually dimorphic neurogenesis is topographically matched with the anterior accessory olfactory bulb of the adult rat. *Cell and Tissue Research*:385-389.

Quast KB, Ung K, Froudarakis E, Huang L, Herman I, Addison AP, Ortiz-Guzman J, Cordiner K, Saggau P, Tolias AS, Arenkiel BR (2017) Developmental broadening of inhibitory sensory maps. *Nature Neuroscience*:189-199.

Restrepo D, Lin W, Salcedo E, Yamazaki K, Beauchamp G (2006) Odortypes and MHC peptides: complementary chemosignals of MHC haplotype? *Trends in Neurosciences*:604-609.

Rosser AE, Keverne EB (1985) The importance of central noradrenergic neurones in the formation of an olfactory memory in the prevention of pregnancy block. *Neuroscience*.

Rothermel M, Brunert D, Zabawa C, Díaz-Quesada M, Wachowiak M (2013) Transgene Expression in Target-Defined Neuron Populations Mediated by Retrograde Infection with Adeno-Associated Viral Vectors. *The Journal of Neuroscience* 33:15195-15206.

Rubin R, Abbott LF, Sompolinsky H (2017) Balanced excitation and inhibition are required for high-capacity, noise-robust neuronal selectivity. *Proceedings of the National Academy of Sciences* 114.

Runyan CA, Sur M (2013) Response Selectivity Is Correlated to Dendritic Structure in Parvalbumin-Expressing Inhibitory Neurons in Visual Cortex. *The Journal of Neuroscience*:11724-11733.

Rupprecht P, Friedrich RW (2018) Precise Synaptic Balance in the Zebrafish Homolog of Olfactory Cortex. *Neuron* 100:669-68300000.

Ryba NJ, Tirindelli R (1997) A new multigene family of putative pheromone receptors. *Neuron* 19:371-379.

- Sailor KA, Valley MT, Wiechert MT, Riecke H, Sun GJ, Adams W, Dennis JC, Sharafi S, Ming G-I, Song H, Lledo P-M (2016) Persistent Structural Plasticity Optimizes Sensory Information Processing in the Olfactory Bulb. *Neuron*:384-396.
- Schoppa NE, Kinzie MJ, Sahara Y, Segerson TP, Westbrook GL (1998) Dendrodendritic Inhibition in the Olfactory Bulb Is Driven by NMDA Receptors. *Journal of Neuroscience* 18:6790-6802.
- Schwaller B (2010) Cytosolic Ca²⁺ Buffers. *Cold Spring Harbor Perspectives in Biology* 2.
- Shinohara H, Asano T, Kato K (1992) Differential localization of G-proteins Gi and Go in the accessory olfactory bulb of the rat. *The Journal of Neuroscience* 12:1275-1279.
- Shiple MT, Adamek GD (1984) The connections of the mouse olfactory bulb: A study using orthograde and retrograde transport of wheat germ agglutinin conjugated to horseradish peroxidase. *Brain Research Bulletin* 12:669-688.
- Smith RS, Hu R, DeSouza A, Eberly CL, Krahe K, Chan W, Araneda RC (2015) Differential Muscarinic Modulation in the Olfactory Bulb. *The Journal of Neuroscience* 35:10773-10785.
- Sohya K, Kameyama K, Yanagawa Y, Obata K, Tsumoto T (2007) GABAergic Neurons Are Less Selective to Stimulus Orientation than Excitatory Neurons in Layer II/III of Visual Cortex, as Revealed by In Vivo Functional Ca²⁺ Imaging in Transgenic Mice. *The Journal of Neuroscience*:2145-2149.
- Stowe MK, Turlings TC, Loughrin JH, Lewis WJ, Tumlinson JH (1995) The chemistry of eavesdropping, alarm, and deceit. *Proceedings of the National Academy of Sciences* 92:23-28.
- Stowers L, Liberles SD (2016) State-dependent responses to sex pheromones in mouse. *Current Opinion in Neurobiology* 38:74-79.
- Su C-Y, Menuz K, Carlson JR (2009) Olfactory perception: receptors, cells, and circuits. *Cell* 139:45-59.
- Symonds M, Elgar MA (2008) The evolution of pheromone diversity. *Trends in Ecology & Evolution*:220-228.
- Taniguchi H, He M, Wu P, Kim S, Paik R, Sugino K, Kvitsiani D, Kvitsani D, Fu Y, Lu J, Lin Y, Miyoshi G, Shima Y, Fishell G, Nelson SB, Huang ZJ (2011) A resource of Cre driver lines for genetic targeting of GABAergic neurons in cerebral cortex. *Neuron* 71.
- Taniguchi M, Kaba H (2001) Properties of reciprocal synapses in the mouse accessory olfactory bulb. *Neuroscience* 108:365-370.

Thoß M, Enk V, Yu H, Miller I, Luzynski KC, Balint B, Smith S, Razzazi-Fazeli E, Penn DJ (2016) Diversity of major urinary proteins (MUPs) in wild house mice. *Scientific Reports* 6:38378.

Tolokh, II, Fu X, Holy TE (2013) Reliable sex and strain discrimination in the mouse vomeronasal organ and accessory olfactory bulb. *J Neurosci* 33:13903-13913.

Tremblay R, Lee S, Rudy B (2016) GABAergic Interneurons in the Neocortex: From Cellular Properties to Circuits. *Neuron* 91:260-292.

Turaga D, Holy TE (2012) Organization of vomeronasal sensory coding revealed by fast volumetric calcium imaging. *J Neurosci* 32:1612-1621.

Verkhatsky A, Shmigol A (1996) Calcium-induced calcium release in neurones. *Cell Calcium* 19:1-14.

Wagner S, Gresser AL, Torello AT, Dulac C (2006) A multireceptor genetic approach uncovers an ordered integration of VNO sensory inputs in the accessory olfactory bulb. *Neuron* 50.

Wall C, Perry JN (1987) Range of action of moth sex - attractant sources. *Entomologia Experimentalis et Applicata* 44:5-14.

Wei Z, Lin B-J, Chen T-W, Daie K, Svoboda K, Druckmann S (2019) A comparison of neuronal population dynamics measured with calcium imaging and electrophysiology. *bioRxiv*:840686.

Wilson EO (1963) Pheromones. *Scientific American*:100-114.

Wilson NR, Runyan CA, Wang FL, Sur M (2012) Division and subtraction by distinct cortical inhibitory networks in vivo. *Nature* 488.

Woodson J, Niemeyer A, Bergan J (2017) Untangling the Neural Circuits for Sexual Behavior. *Neuron* 95:1-2.

Yoles-Frenkel M, Kahan A, Ben-Shaul Y (2018) Temporal Response Properties of Accessory Olfactory Bulb Neurons: Limitations and Opportunities for Decoding. *The Journal of neuroscience : the official journal of the Society for Neuroscience* 38:4957-4976.

Yoshinaga S, Sato T, Hirakane M, Esaki K, Hamaguchi T, Haga-Yamanaka S, Tsunoda M, Kimoto H, Shimada I, Touhara K, Terasawa H (2013) Structure of the mouse sex peptide pheromone ESP1 reveals a molecular basis for specific binding to the class C G-protein-coupled vomeronasal receptor. *The Journal of biological chemistry* 288:16064-16072.

Zhu P, Frank T, Friedrich RW (2013) Equalization of odor representations by a network of electrically coupled inhibitory interneurons. *Nature Neuroscience* 16:1678-1686.

Znamenskiy P, Kim M-H, Muir DR, Iacaruso M, Hofer SB, Mrsic-Flogel TD (2018) Functional selectivity and specific connectivity of inhibitory neurons in primary visual cortex. bioRxiv:294835.